

MULTI-LAYER INAS/GAAS QUANTUM-DOT INFRARED
PHOTODETECTOR WITH HIGH QUANTUM EFFICIENCY

BY

HAIYAN ZHANG
B.S. SOUTHEAST UNIVERSITY, CHINA (2007)

SUBMITTED IN PARTIAL FULFILLMENT OF THE REQUIREMENTS
FOR THE DEGREE OF MASTER OF SCIENCE
DEPARTMENT OF ELECTRICAL AND COMPUTER ENGINEERING
UNIVERSITY OF MASSACHUSETTS LOWELL

Signature of

Author: Haiyan Zhang Date: 07/16/2010

Signature of Thesis

Supervisor: 07/27/2010

Name Typed:

Xuejian Lu

Signatures of Other Thesis Committee Members:

Committee Member Signature:

Name Typed: Joel Therrien

Committee Member Signature:

Name Typed: Craig Armiento

Committee Member Signature:

Name Typed:

UMI Number: 1486586

All rights reserved

INFORMATION TO ALL USERS

The quality of this reproduction is dependent upon the quality of the copy submitted.

In the unlikely event that the author did not send a complete manuscript and there are missing pages, these will be noted. Also, if material had to be removed, a note will indicate the deletion.



UMI 1486586

Copyright 2010 by ProQuest LLC.

All rights reserved. This edition of the work is protected against unauthorized copying under Title 17, United States Code.



ProQuest LLC
789 East Eisenhower Parkway
P.O. Box 1346
Ann Arbor, MI 48106-1346

**MULTI-LAYER INAS/GAAS QUANTUM-DOT INFRARED
PHOTODETECTOR WITH HIGH QUANTUM EFFICIENCY**

BY

HAIYAN ZHANG

**ABSTRACT OF A THESIS SUBMITTED TO THE FACULTY OF THE
DEPARTMENT OF ELECTRICAL AND COMPUTER ENGINEERING
IN PARTIAL FULFILLMENT OF THE REQUIREMENTS
FOR THE DEGREE OF
MASTER OF SCIENCE
UNIVERSITY OF MASSACHUSETTS LOWELL
2010**

Thesis Supervisor: Xuejun Lu, Ph.D.

Associate Professor, Department of Electrical and Computer Engineering

ABSTRACT

In the past decade, Quantum Dots Infrared Photodetectors (QDIPs) are playing an increasingly important role in diverse application fields, such as night vision, thermal imaging, remote sensing and space exploration. But their performances are still restricted by the relatively low quantum efficiency (QE) of $\sim 1\% - 3\%$ due to the limitation on the active thickness. In this thesis, a normal-incidence, long-wavelength infrared (LWIR) QDIP with 20 periods of InAs-InGaAs quantum dots layers is demonstrated and discussed in details. A high quantum efficiency of 11.7% is obtained under the operating temperature of 78K with a bias of -4.8V. QDIPs with higher QE are expected by repeating more quantum dots layers, which allow a better sensitivity to MWIR (mid-wavelength infrared) and LWIR radiations.

ACKNOWLEDGEMENT

First and foremost, I would like to thank my wonderful parents who I owe the most gratitude. They give me endless love and comfort which encourage me all the time. Without their dedication and support, I wouldn't go this far.

I am also heartily thankful to my supervisor, Professor Xuejun Lu, whose guidance and support from the initial to the final level enabled me to develop an understanding of this subject. During my research time, I learned and developed my skills by the mistakes I made. Without countless opportunities he gave me, I would not have been able to finish this thesis. Apart from the research, he has been so kind for all time.

In addition, I would like to thank my group members, Pete, Jarrod, Ruby, and Runyu, for being there with me every step of the way. I know I could have never completed this thesis without their help and hard work.

Lastly, I would like to thank the committees, Professor Craig Armiento and Professor Joel Therrien, for their time and effort to review my thesis. Their useful comments are very grateful.

TABLE OF CONTENTS

ABSTRACT.....	iii
ACKNOWLEDGEMENT	iv
TABLE OF CONTENTS.....	v
LIST OF TABLES.....	viii
LIST OF ILLUSTRATIONS.....	ix
I. Introduction	1
1.1 Infrared Radiation	1
1.2 Applications of Infrared radiation	3
Night vision	3
1.3 Infrared Detectors.....	6
1.3.1 Infrared Thermal Detector.....	7
1.3.2 Infrared Quantum Detector.....	10
1.4 Work of this thesis.....	14
II. Material Growth and Device Fabrication.....	16
2.1 Material Growth	16
2.2 Photoluminescence Measurement (PL).....	18
2.3 Device fabrication	21
III. Device Characterization.....	25
3.1 Fourier Transform Infrared (FTIR) test	25

3.1.1 FTIR test set up.....	25
3.1.2 FTIR test result	27
3.2 Dark Current test	29
3.2.1 Dark Current test set up.....	29
3.2.2 Dark current test result	30
3.2.3 Noise current test	32
3.3 Photocurrent test.....	35
3.3.1. Photocurrent test set up.....	35
3.3.2. Photocurrent test results:	36
3.4 Photoconductive Gain	37
3.5 Photoresponsivity	39
3.6 Photodetectivity.....	40
3.7 Quantum Efficiency	41
IV. Comparison and Discussion	50
4.1 10-period sample #2783	50
4.2 FTIR Performance:.....	51
4.3 Dark Current Comparison	52
4.4 Photoconductive gain comparison:	53
4.5 Photoresponsivity Comparison	54
4.6 Photodetectivity Comparison	55

4.7 Quantum Efficiency Comparison.....	56
V. Conclusion and Future Work	58
VI. Literature Cited.....	59
VII. Biographical Sketch of Author.....	61

LIST OF TABLES

Table 1 Types of infrared detectors	6
Table 2 test data for #2797 under 78 K.....	34
Table 3 test data for #2797 under 78K.....	36

LIST OF ILLUSTRATIONS

Figure 1 the Infrared Bands in the Electromagnetic Spectrum.....	2
Figure 2 Active – infrared night vision camera	3
Figure 3 IR Satellite picture taken 1315 Z on 15th October 2006.....	5
Figure 4 Diagram of photon absorption in semiconductor	10
Figure 5 Schematic layers of a QWIP and QDIP	12
Figure 6 Schematic potential profile for both QWIP and QDIP under bias	12
Figure 7 the schematic structure for 20-layer sample #2797	17
Figure 8 the schematic PL measurement band diagram	19
Figure 9 PL test result	20
Figure 10 QDIP Fabrication procedures	23
Figure 11 QDIP devices with wire bondings	24
Figure 12 Schematic Illustration of FTIR System	25
Figure 13 FTIR test set up in CEMOS lab.....	26
Figure 14 FTIR response for sample #2797 under 78K – positive bias	27
Figure 15 FTIR response for sample #2797 under 78K – negative bias	28
Figure 16 Dark current test set up in CEMOS lab	29
Figure 17 Dark Current Density for #2797 – linear scale.....	30
Figure 18 Dark Current Density for #2797 – log scale.....	31
Figure 19 Noise current test set up in CEMOS lab.....	32
Figure 20 Photocurrent test set up in CEMOS lab.....	35
Figure 21 Explanation for Photoconductive Gain	37
Figure 22 Conductive gain for #2797 under 78K`	38

Figure 23 Photoresponsivity for #2797 under 78K.....	39
Figure 24 Detectivity for #2797 under 78K.....	41
Figure 25 Quantum Efficiency for #2797 under 78K.....	43
Figure 26 Diagram of Beer-Lambert absorption	44
Figure 27 $\ln(1-\text{QE})$ Vs Voltage.....	45
Figure 28 $\ln(1/\text{QE}-1)$ Vs Voltage	47
Figure 29 Diagram of the QDIP with bias voltage	48
Figure 30 the schematic structure for 10-layer sample #2783	50
Figure 31 FTIR response for sample #2783 under 78K	51
Figure 32 Dark current comparison	52
Figure 33 Photoconductive Gain Comparison.....	54
Figure 34 Responsivity Comparison.....	55
Figure 35 Photodetectivity Comparison	56
Figure 36 Quantum Efficiency Comparison	57

I. Introduction

1.1 Infrared Radiation

Electromagnetic radiation can be considered as a stream of photons (massless particles) traveling at the speed of light (300,000,000 meters per second), and propagating in the formation of wave – like patterns.

In the entire electromagnetic spectrum, Infrared Radiation (IR) is made up of many frequencies and wavelengths, locating between the visible light and terahertz radiation microwaves. The wavelength of Infrared Radiation is between 0.7 and 300 micrometers, which roughly equates to a frequency range between 1 and 430 THz.

The IR spectrum can be roughly subdivided into 5 regions(1), which are:

- 1) Near Infrared (NIR) band, ranging from 0.7 – 1.0 um, mainly works in fiber optical telecommunication systems.
- 2) Short Wave Infrared (SWIR) band, ranging from 1.0 – 3.0 um, mainly works in the long-distance telecommunications (remote sensing).
- 3) Medium Wavelength Infrared (MWIR) band, ranging from 3.0 – 5.0 um
- 4) Long Wavelength Infrared (LWIR) bands, ranging from 8 – 12 um

Both (3) and (4) have been applied in Infrared Thermography for military or civilian area, such as target signature identification, surveillance, nondestructive evaluation, etc.

5) Very Long Wavelength Infrared (VLIR) band, ranging from 14 – 300 μm , mainly works in spectroscopy and astronomy area.

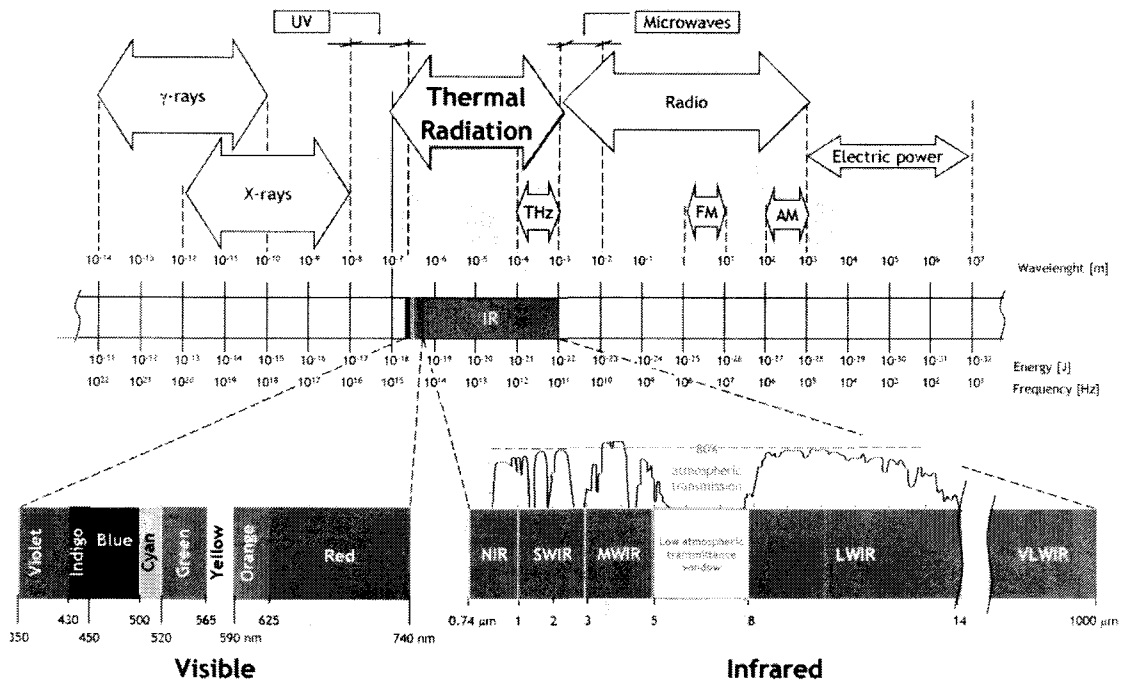


Figure 1 the Infrared Bands in the Electromagnetic Spectrum

* Image from http://en.wikipedia.org/wiki/Infrared_vision. Author: Clemente Ibarra-Castanedo @ Canada Research Chair in Multipolar Infrared Vision - MiViM

1.2 Applications of Infrared radiation

Infrared radiation plays an important role in diverse application fields, such as missile guidance, night vision, and surveillance in the military fields; satellite detection, space observation, space vehicle navigation flight controller in space exploration. Infrared radiation also plays an important role in some civilian fields, including optical communication, weather satellite, remote control, and thermography camera. (2-4)

Night vision

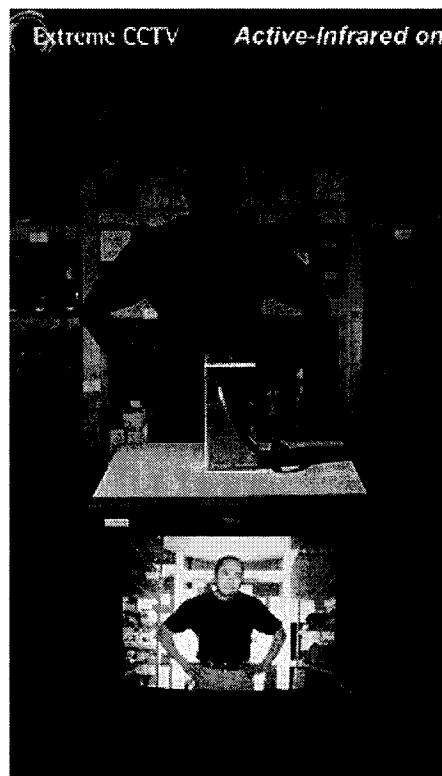


Figure 2 Active – infrared night vision camera

*Image form www.extremeCCTV.com

Infrared radiation can be used in night vision equipment in the situation where the visible light is insufficient for the human eye to see something clearly(5). Night vision equipment can convert light photons into electrons, which are then amplified by some

chemical or electrical process, and then converted back into visible light. Infrared light sources can be used to increase the in-the-dark visibility without actually using a visible light source. As what is showed in the figure 2, the active-infrared night vision delivers identifying details as seen on the display monitor, despite a dark back-lit scene.

Tracking

Infrared tracking refers to a passive missile guidance system, which uses the infrared part of electromagnetic radiation from a target to track it. Missiles which use infrared seeking are also called as “heat-seekers”, since infrared light radiated strongly by hot bodies. Therefore, many objects such as people, vehicle engines and aircraft are more visible in the infrared wavelengths of light compared with other objects in the background, since they retain more heat(6).

Communications

IR data transmission is widely used in the short-range communication among computer peripherals and personal digital assistants. These Infrared Data Association devices use infrared LEDs to emit infrared radiation which is focused into a narrow beam by a plastic lens. The beam will be modulated to encode the data. The receiver uses a silicon photodiode to convert the infrared radiation to an electric current. Infrared communications are especially useful for indoor areas with high population density. It is the most common way for remote controls to command appliances.

Meteorology

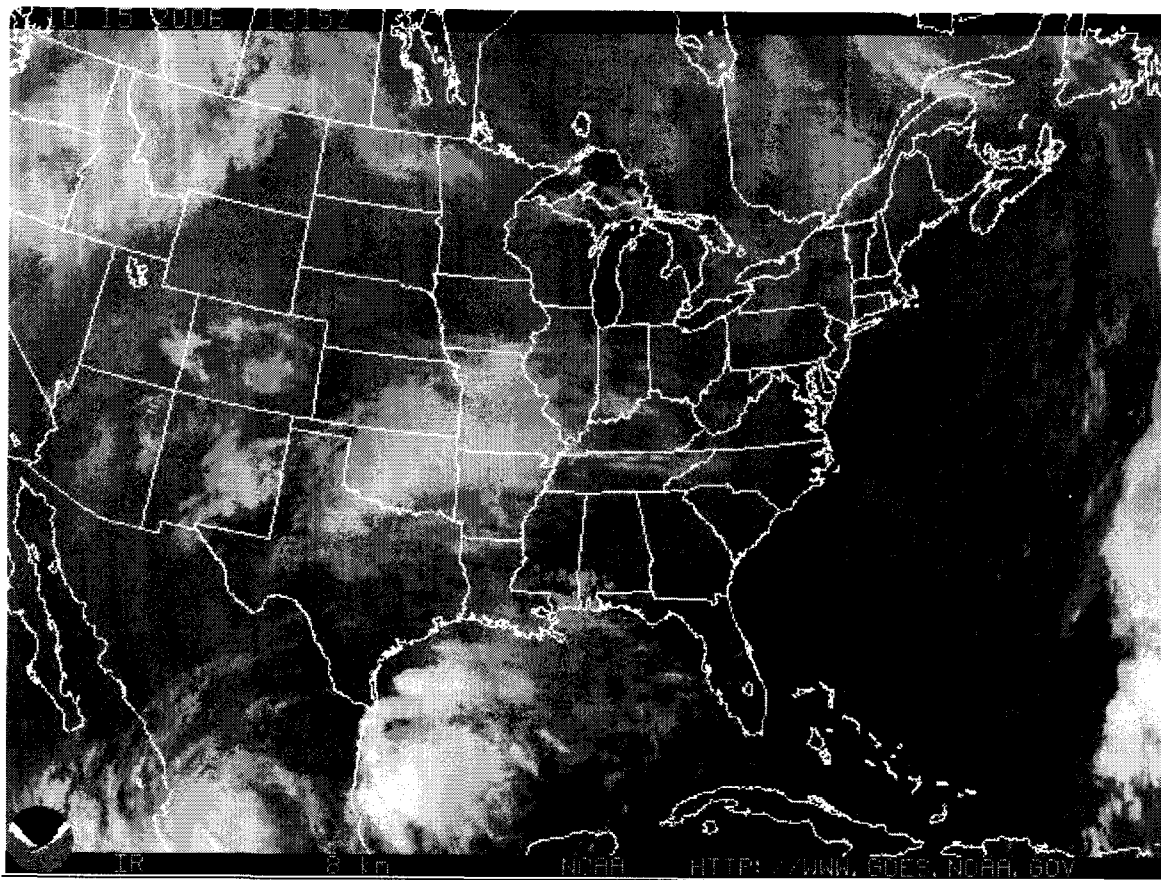


Figure 3 IR Satellite picture taken 1315 Z on 15th October 2006

**Image from the National Oceanic and Atmospheric Administration*

Weather satellites equipped with scanning radiometers produce thermal or infrared images, which can enable people to determine cloud heights and types, to calculate land and surface water temperatures, and to locate ocean surface features. These infrared pictures can also depict ocean eddies or vortices and map currents such as the Gulf Stream which are valuable to the shipping industry. The main advantage of infrared is that images can be produced at night, allowing a continuous sequence of weather to be studied.

1.3 Infrared Detectors

Type		Detector	Spectral Response (μm)	Operating Temperature (K)	$D^*(\text{cm} \cdot \sqrt{\text{Hz}} / \text{W})$	
Thermal type	Thermocouple Thermopile	Golay cell PZT,TGS	Depends on window material	300	$D^*(\lambda, 10, 1) = 6 \times 10^8$	
	Bolometer			300	$D^*(\lambda, 10, 1) = 1 \times 10^8$	
	Pneumatic cell			300	$D^*(\lambda, 10, 1) = 1 \times 10^9$	
	Pyroelectric detector			300	$D^*(\lambda, 10, 1) = 2 \times 10^8$	
Quantum type	Extrinsic type		Ge:Au	1 to 10	$D^*(500, 900, 1) = 1 \times 10^{11}$	
			Ge:Hg	2 to 14	$D^*(500, 900, 1) = 8 \times 10^9$	
			Ge:Cu	2 to 30	$D^*(500, 900, 1) = 5 \times 10^9$	
			Ge:Zn	2 to 40	$D^*(500, 900, 1) = 5 \times 10^9$	
			Si:Ga	1 to 17	$D^*(500, 900, 1) = 5 \times 10^9$	
			Si:As	1 to 23	$D^*(500, 900, 1) = 5 \times 10^9$	
	Photoconductive type	PbS	1 to 3.6	300	$D^*(500, 600, 1) = 1 \times 10^9$	
		PbSe	1.5 to 5.8	300	$D^*(500, 600, 1) = 1 \times 10^8$	
		InSb	2 to 6	213	$D^*(500, 1200, 1) = 2 \times 10^9$	
		HgCdTe	2 to 16	77	$D^*(500, 1000, 1) = 2 \times 10^{10}$	
	Intrinsic type	Photovoltaic type	Ge	0.8 to 1.8	$D^*(\lambda p) = 1 \times 10^{11}$	
			InGaAs	0.7 to 1.7	$D^*(\lambda p) = 5 \times 10^{12}$	
			Ex. InGaAs	1.2 to 2.55	$D^*(\lambda p) = 2 \times 10^{11}$	
			InAs	1 to 3.1	$D^*(500, 1200, 1) = 1 \times 10^{10}$	
			INsB	1 to 5.5	$D^*(500, 1200, 1) = 2 \times 10^{10}$	
			HgCdTe	2 to 16	$D^*(500, 1000, 1) = 1 \times 10^{10}$	

Table 1 Types of infrared detectors

(From Characteristics and use of infrared photodetectors, Hamamatsu)

Infrared radiation can be widely used in diverse civilian and military fields as mentioned in Chapter 1.2. With the rapid development of photonics technology, a wide variety of infrared detectors are now available in order to meet a large range of application needs. There are two main categories of infrared detectors - thermal models and quantum models(7). The former detector mainly depends on the energy of the infrared beam as heat, and its photo sensitivity is not related with wavelength; while the latter mainly depends on semiconductor quantum, and its photo sensitivity is related with wavelength. Generally speaking, the most advantage of thermal detectors is they are able to operate at room temperature, but they have relatively low detectives and slow response due to the slow process of heating and cooling of the detectors. On the other hand, quantum detectors offer a higher detectivity and faster response speed, but they usually need to be cooled down in order to cut down thermal noises.

1.3.1 Infrared Thermal Detector

According to different temperature related phenomena, thermal detectors can be divided into several categories: bolometers base on changes in resistance; thermocouples and thermopiles relate to thermoelectric effect; Golay cells follows thermal expansion; and pyroelectric detectors depend on the changes in the temporary electric potential.

Bolometer

A bolometer consists of a thin layer of metal, a heat sink, and an insulating link between them. The thin layer of metal can absorb electromagnetic radiation, and then affect the temperature of the heat sink via the insulating link – the more radiation it

absorbed, the higher the temperature will be. Since the change of the temperature can be directly measured, bolometer can be used to measure radiation energy of any frequency. For most wavelength ranges, there are other types of detectors that are more accurate and efficient, but for sub-millimeter range (around $200\mu\text{m}$ – 1 mm), bolometer can be considered as the most sensitive one. They can be used for any sort of radiation, even to search for unknown forms of mass or energy. However, this lack of discrimination can also be a shortcoming, and they also suffer from slow respond and slow reset.

Thermocouple

A thermocouple is a junction between two different metals, which can create a voltage related to temperature difference. For specific alloys, the relationship between voltage and temperature is predictable and repeatable, thus thermocouples can be widely used to measure and control temperature, as well as convert heat into electric power. Thermocouples are inexpensive and interchangeable. And at the same time, they can measure a wide range of temperatures. The main limitation is its sensitivity: it will be very hard to get a detection resolution which is less than 1 Kelvin.

Thermopile

A thermopile is composed of thermocouples, which are connected in series, or occasionally in parallel. Instead of measuring the absolute temperature, thermopiles generate an output voltage proportional to a local temperature difference or temperature gradients. The ear thermometer, which is a kind of thermopile, is widely used by doctors to measure body temperature. Thermopiles are also widely used in the area of heat flux

sensors and gas burner safety controls. The disadvantage is that the output voltage is very small, usually in the order of tens or hundreds of millivolts, therefore it requires amplifiers which can be very large and expensive.

Golay Cell

Golay Cell consists of a small metal cylinder which is filled with xenon. On one end of the cylinder is a blackened metal plate, which is used to absorb the IR radiation; and on the other end is a flexible metalized diaphragm, which is used to reflects the light to a photocell . When IR radiation falls on the blackened metal plate, the xenon gas got heated and then expand, which will lead to the deformation of the diaphragm. The motion of the diaphragm will change the output of the cell. In this way, we can detect the infrared spectroscopy.

Pyroelectric detector

When certain materials are heated or cooled, their atoms' positions will slightly change within the crystal structure, therefore the polarization of the material changes. This change will generate a temporary electric potential, although this potential will disappear after some dielectric relaxation time. Due to this specific characteristic - pyroelectricity, passive infrared detectors are designed. Those detectors could be very sensitive to radiations over a wide range, and they are also relatively inexpensive and easy to use.

1.3.2 Infrared Quantum Detector

The main operation mechanism for quantum detectors is based on the photo excitation of electrons(8). There are two types of electron transition, interband transition and intersubband transition.

For the interband transition based photodetectors, the excitation happens only if the photon energy is greater than the bandgap of semiconductor material such as Si or GaAs. The working diagram of interband transition could be illustrated in Figure 4 : by absorbing the energy from incident photons, a free electron is moved to the conduction band, while a hole is left in the valence band. The electron – hole pairs will be collected and form the photocurrent. In this way, an infrared quantum detector converts an electromagnetic wave signal into an electrical signal.

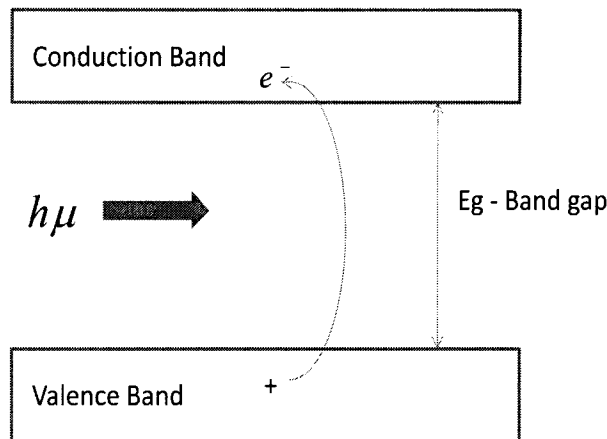


Figure 4 Diagram of photon absorption in semiconductor

The relationship between photon energy and wavelength can be described as follows:

$$E = h \mu = \frac{hc}{\lambda}$$

E is the energy of the photon

h is the Plank's constant

μ is the frequency of light

c is the speed of light

λ is the wavelength of the light

The second type is the intersubband transition based photodetectors. Due to the quantum confinement in quantum wells and quantum dots, the photon excitation results in either the electron transitions within the conduction band or the hole transitions within the valance band, as shown in figure6. For a rectangular quantum well potential, the conduction band of the QWs and QDs are split into discrete energy levels, which could be described as:

$$E_n = \frac{\hbar^2 \pi^2}{2m^* L^2} \cdot n^2$$

m^* is the effective mass of the electron

L is the width of the quantum well

n is the discrete energy level

\hbar is the reduced Planck constant

Two typical examples are quantum well infrared photodetector (QWIP) and quantum dot infrared photodetector (QDIP). Based on mature GaAs materials and

fabrication technology, the area of QWIP and QDIP research is very attractive, and a lot of significant progresses are made during the past few years.

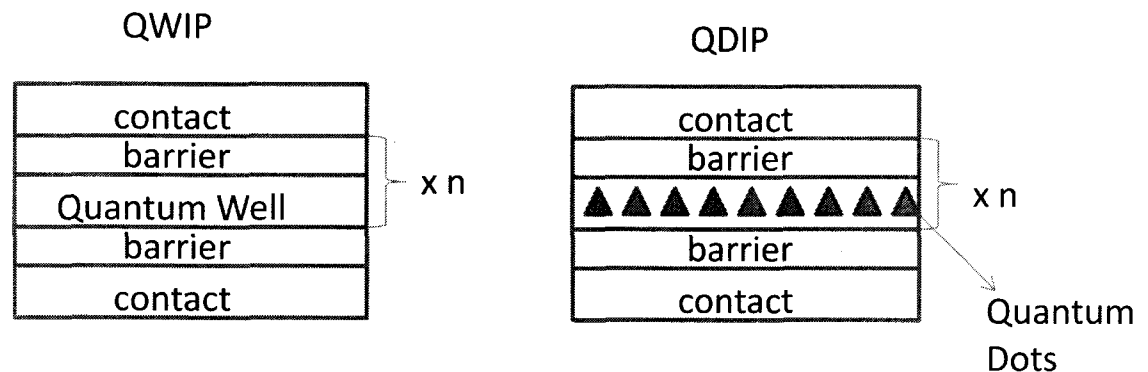


Figure 5 Schematic layers of a QWIP and QDIP

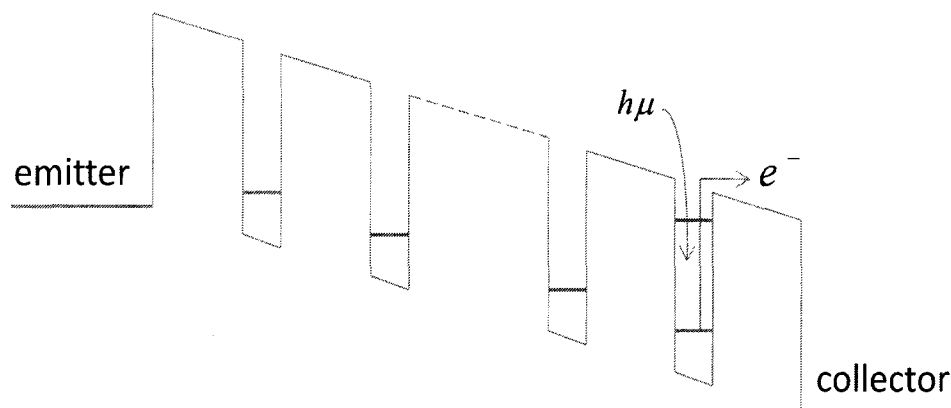


Figure 6 Schematic potential profile for both QWIP and QDIP under bias
(Intersubband transition)

1.3.2.1 QWIP

The detection mechanism in QWIPs can be explained in Fig 6: when the incident light shines on the detectors, electrons from confined state in conduction band wells will absorb certain photon energy, and excite to a higher energy level near continuum band. With some applied voltage bias, electrons will tunnel through potential barriers to the continuum band, and then get collected as photocurrent.

At present, QWIPs are being commercialized for infrared imaging applications. Other areas such as high-speed detection may also find practical applications. Compared with other infrared detectors, QWIPs have several advantages such as low cost, good uniformity, higher sensitivity with wavelength flexibility and multicolor capability. But on the other hand, they suffer from higher dark current and lack of normal incidence absorption and require cryogenic operation temperature.

1.3.2.2 QDIP

Generally speaking, QDIPs are similar to QWIPs with the quantum wells replaced by quantum dots, as what is shown in Fig 5. An ideal QDIP is expected to be potentially superior than QWIP in the following areas(9):

1. QDIPs have 3-dimensional quantum confinement, while QWIPs have only 1-dimensional confinement. The 3-dimensional quantum confinement provides the ability to absorb normally incident light due to the requirement of quantum selection rules(10), which leads to a more effective intersubband transition in the conduction band. The normal incident detection allows us to remove the need for special light coupling techniques such as gratings, making the fabrication of the photodetectors less complicated.

2. Due to much lower density of states, Quantum Dots can capture much less thermally-generated electrons, and therefore much less dark current than Quantum Wells. And at the same time, quantum dots would be less temperature sensitive due to the reduced dependence of the density of states on temperature.
3. The carrier lifetime of QDIPs is around 10 – 100 times longer than that of QWIPs, which provides the potential for more efficient photon absorption, and a higher photoconductive gain and photoresponsivity.

However, one of the major drawbacks of QDIPs is its relatively low quantum efficiency due to the nonuniformities in the quantum dots size and the limitations in the quantum dots density because of some filling factor reasons(11). The common value of quantum efficiency for QWIPs is around 20% while it is only 1% for QDIPs, published in prior report. The low QE greatly restricts the light sensitivity of the device, and limits their further applications. Therefore, how to improve the quantum efficiency of QDIPs becomes a main objective of this thesis.

1.4 Work of this thesis

This thesis tries to improve the quantum efficiency of QDIPs by repeating 20 quantum dots layers. The self-assembled InAs quantum dots and the wafer structure were grown by MBE method under Stranski-Krastanov (SK) mode, while the photodetector device was fabricated in Harvard CNS cleanroom with conventional photolithography method. A peak detection wavelength of 8 micron is reported. A large photodetectivity of

$9.95 \times 10^9 \text{ cm} \cdot H_z^{1/2} / W$ and a high peak quantum efficiency of 11.7% were obtained at the operating temperature of 78 K, with a bias voltage of -2.8V and -4.8V, respectively.

A previous 10 layer quantum dot infrared photodetector with the same peak detection wavelength was introduced to help better evaluation those characteristics. After comparison, it is obvious that the performance was greatly enhanced by increasing the number of quantum dots layers, from 10 layers to 20 layers. A higher quantum efficiency could be expected by incorporating more quantum dot layers. Since the QDIPs have long been suffered from low quantum efficiency, around 1% in the prior reports (11), it is worth identifying reasons for QDIPs to perform far below expectations. This conclusion is shown to be attributable to the development of QDIPs.

The author also analyzed the relationship between quantum efficiency, absorption coefficient and bias voltage. The absorption coefficient could be considered the same at different bias voltages. However, while the bias voltage increases to a relatively high value, the effect of the escape probability could not be neglected, so that the total net quantum efficiency appears to rise with the bias voltage. The barrier layer would help to eliminate the increase of the escape probability.

II. Material Growth and Device Fabrication

2.1 Material Growth

Molecular beam epitaxy (MBE) is one of the common methods to deposit single crystals on the substrate. Self – organized quantum dots devices, such as QWIPs and QDIPs are usually grown by this MBE method under Stranski-Krastanov (SK) mode. During the MBE process, the size and the shape of the quantum dots can be determined by many factors, such as grown material, growth temperature, growth interruptions, and growth rate.

While growing QDIP wafers, some key issues should be well considered. The choice of quantum dots is important, since better confined QDs, such as InAs, with stronger potential well also means a higher activation energy, which makes them harder to extract; while easier extracted QDs, such as InGaAs, are more suitable for fabricating VLWIR devices, but the dark current are always higher due to the smaller activation energy. Another trade-off is the doping level inside the quantum dots. Higher doped QDs will increase the absorption quantum efficiency, but also increase the dark current since the excited state are also filled even at a low temperature. The choice of capping layer is also very important. A good capping material will reduce the intermixing of two different materials between the quantum dots and capping layer, and therefore the shape will be preserved and the quantum will be better confined.

Here we choose the DWELL heterostructure, which has been widely studied by many research groups. As displayed in Figure 7, InAs quantum Dots are doped in an InGaAs quantum well. Wetting layers are undoped in order to reduce the dark current. The main benefits of DWELL heterostructure are as follows: precise control over

wavelengths can be realized by altering the ingredients and width of the well; the capture of the carriers will be more efficient due to the quantum well; InGaAs capping layer can be grown at lower temperature, giving rise to a better optical quality.

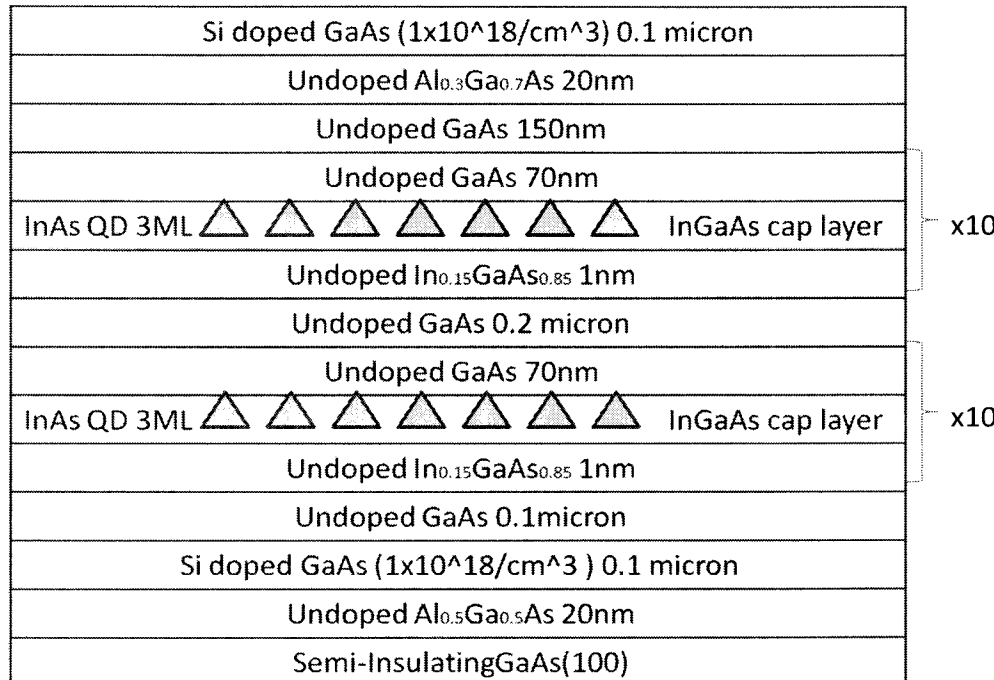


Figure 7 the schematic structure for 20-layer sample #2797

From the schematic picture displayed above, we can see clearly that this LWIR QDIP consists of twenty periods of QD heterostructures between the two Si doped GaAs contacting layer. Each period consist three monolayers(ML) of InAs quantum dots, 70 nm undoped GaAs capping layer and 1 nm undoped In_{0.15}Ga_{0.85}As layer . This structure also contains undoped GaAs buffer layers in order to deposit quantum dots more evenly.

The QDIP structure (#2797) was grown by University of New Mexico, using a Veeco GEN II MBE system(12). A 100 nm undoped Al_{0.5}Ga_{0.5}As layer was doped for selective etching, on the substrate of a semi-insulating GaAs (100) wafer. Then a 0.3 micron highly Si doped ($1 \times 10^{18} /cm^3$) GaAs bottom contacting layer was grown, followed by 0.1 micron undoped GaAs buffer layer. The growth temperature for GaAs contact and buffer layers was set at 610 °C. 10 periods of InAs quantum dots absorption band (3 ML) with 70nm undoped GaAs layer and 1 nm undoped In_{0.15}Ga_{0.85}As layer was then grown at 510 °C . After that, a 0.2 micron undoped GaAs layer was grown, followed by another 10 periods of InAs quantum dots absorption band. Then a 150 nm undoped GasAs buffer layer and a 20 nm undoped Al_{0.5}Ga_{0.5}A layer was grown. The highly Si doped ($1 \times 10^{18} /cm^3$) GaAs top contacting layer was the last expitaxy step. The size and density of QD are measured by atomic force microscopy (AFM), and cross-section transmission electron microscopy (XTEM), which are around 25 nm and $2.9 \times 10^{10} cm^2$, respectively.

2.2 Photoluminescence Measurement (PL)

Photoluminescence(PL) is a photoexcitation process(13) as what is shown in figure 8. At first, the electrons in the valence band are excited to the conduction band by absorbing incident electron magnetic radiations, creating electron-hole pairs. Then the EHPs slowly diffuse until they are captured by quantum dots. Electrons will return to a lower energy state, accompanied by the emission of a photon.

Based on this phenomenon, Photoluminescence Spectroscopy is invented to measure the energy levels of those quantum dots. PL measurement is usually set after MBE growth and before device fabrication, to evaluate the quality of MBE growth.

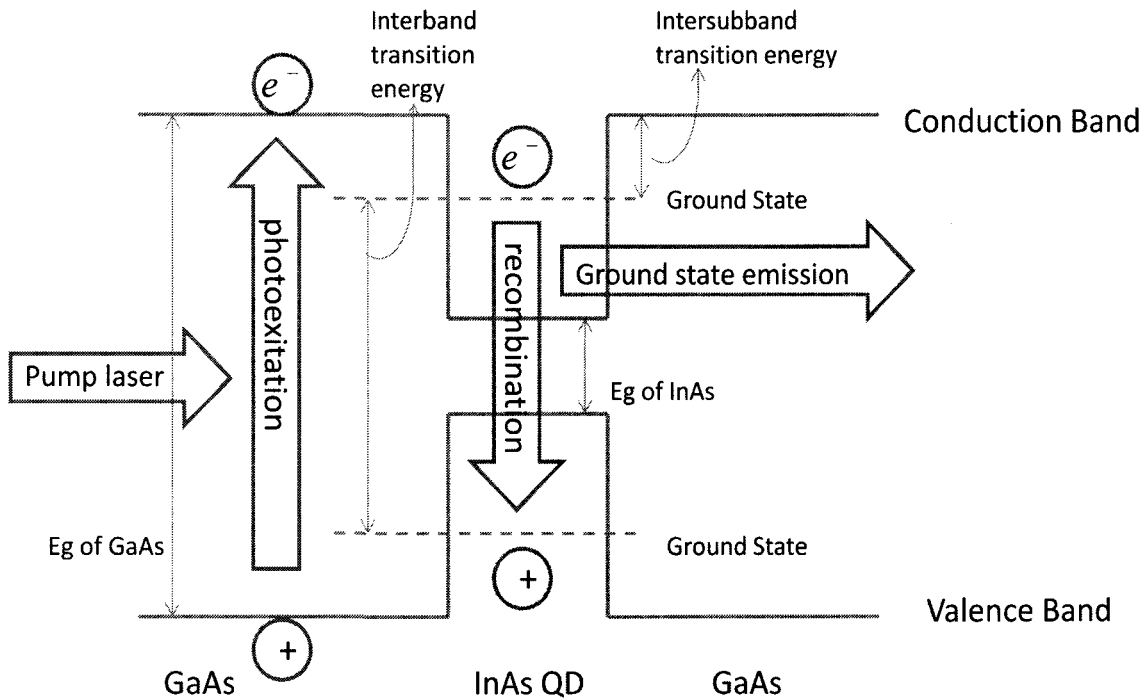


Figure 8 the schematic PL measurement band diagram

The PL test for #2797 was finished by Ms. Hong Wen in our group. With radiation from a continuous wave diode pumped solid state laser (DPSS), the QDIP sample was measured at room temperature. The output of the laser is 200 mW, while the laser spot size is around 0.5mm^2 . A chopper with a frequency of 500Hz is applied in order to eliminate 1/f noise. InGaAs detector, which was cooled by Liquid Nitrogen, was set to detect the reemission signal.

The result was shown in Figure 9. From the graph; we can clearly see that the peak wavelength falls on the wavelength of 1070 nm. According to the equations mentioned in Chapter 1.3.2, we can get the interband transition energy:

$$E = \frac{hc}{\lambda} = \frac{(4.136 \times 10^{-15} \text{ eV}\cdot\text{s}) \times (3 \times 10^8 \text{ m/s})}{1060 \text{ nm}} = 1.171 \text{ eV}$$

At 78K, the band gap of GaAs is 1.507 eV and the bandgap of InAs is 0.405 eV. According to the band diagram in Figure 8, we can get the intersubband transition gap, which equals to half of the difference between the band gap of GaAs and interband transition energy, approximately 0.168 eV. Thus we can get the emission wavelength is around 7.4 micrometers. This result has been verified by our FTIR measurement mentioned in Chapter 3.1.

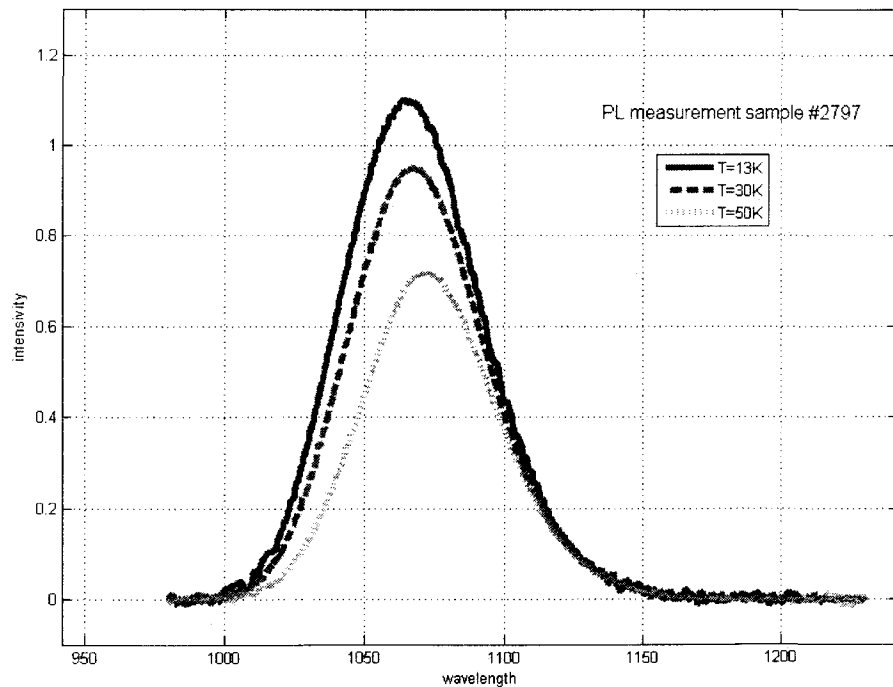
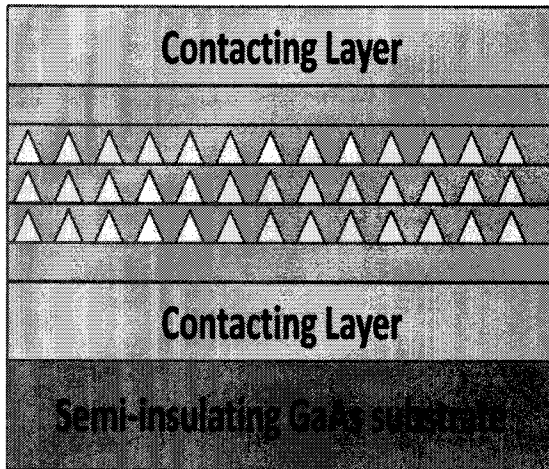


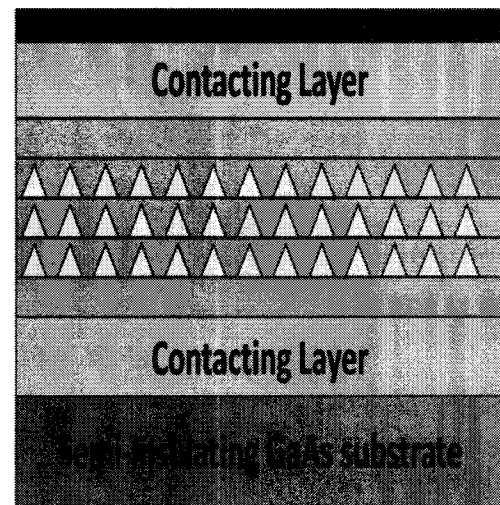
Figure 9 PL test result

2.3 Device fabrication

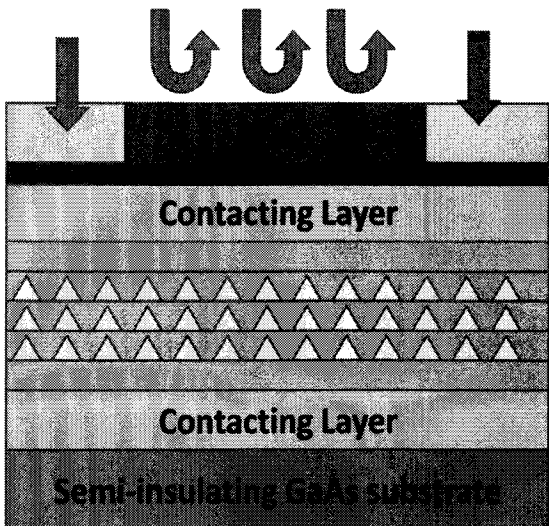
After MBE growth, the wafer is processed into circular mesas in LISE cleanroom, Harvard University, using standard photolithography and wet – etching method. The detailed steps are shown as follows(14):



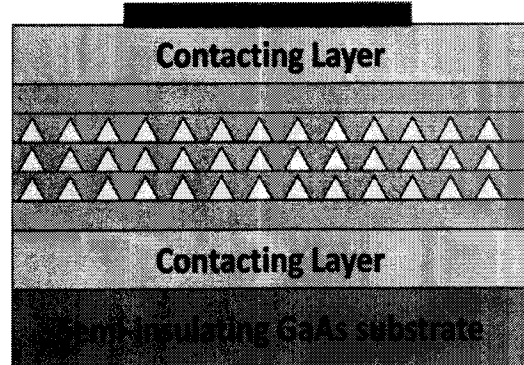
(a)



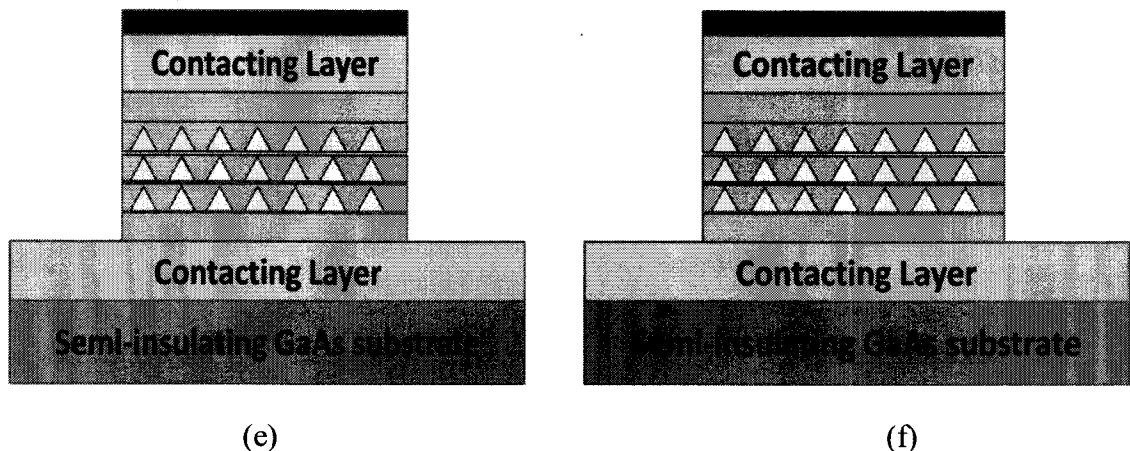
(b)



(c)

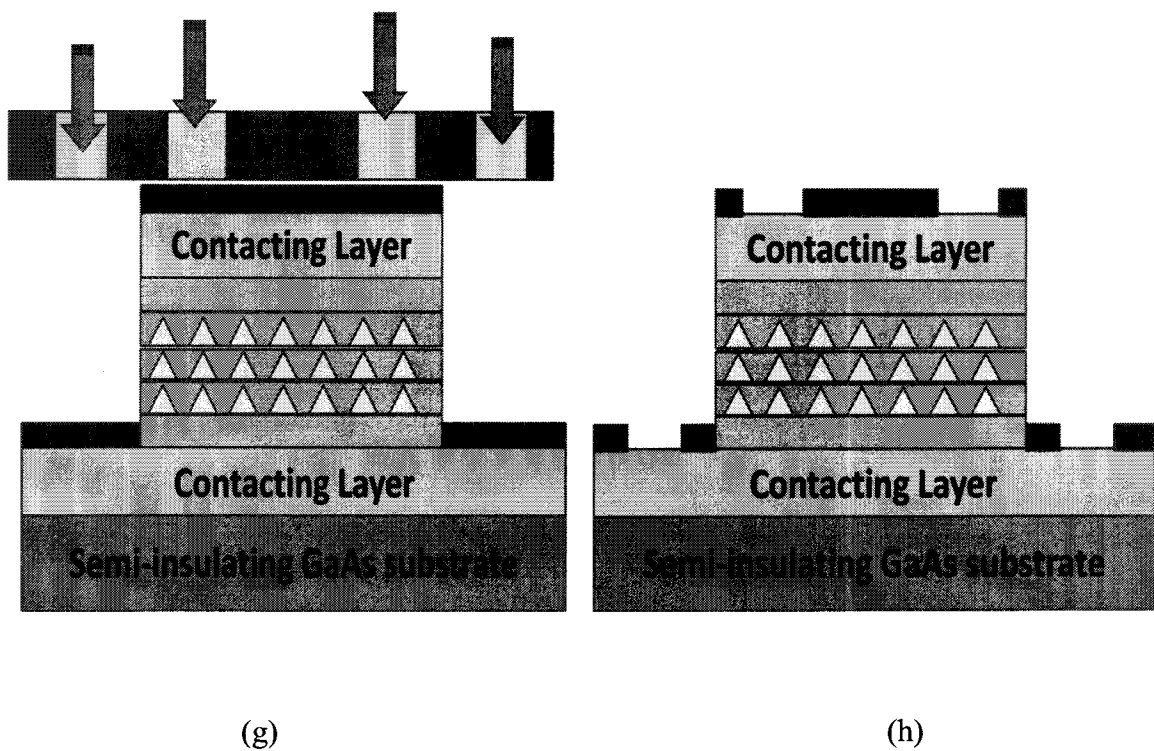


(d)



(e)

(f)



(g)

(h)

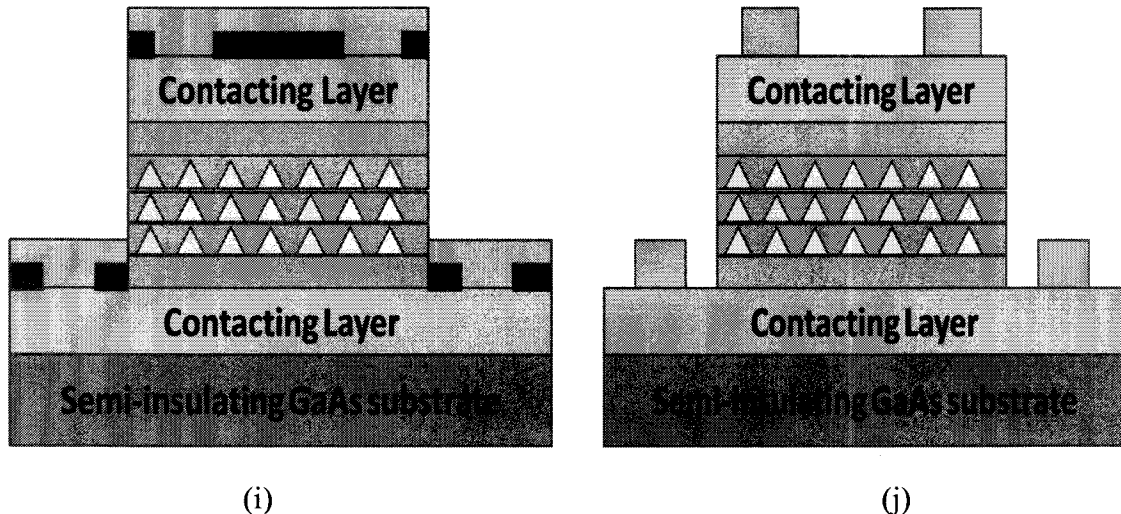


Figure 10 LWIR QDIP Fabrication procedures

**Image from master's thesis, author: Puminun Vasinajindakaw*

At the beginning, the wafer (a) is cleaned and then spin-coated by positive photoresist (b). After soft bake procedure, the wafer will be exposed in UV light under a mesa mask(c). Then the wafer will be put inside a chemical developer. The area where photoresist contacted the UV light will be dissolved (d). In this way, mesa patterns are transferred on the wafer, and selective etching will be realized. With mixture solution of sulfuric acid and hydrogen peroxide, the part without photoresist protection will be etched down till the Si doped GaAs contacting layer (e). The following procedures aim at processing the electrodes. After similar photoresist application(f) and soft bake steps as mentioned above, the wafer will be aligned with another electrode mask(g), followed by

the UV exposure and develop step again(h). Then the electrode pattern will appear on the wafer. After that, a conventional N-type alloy will be deposited on the top of the wafer by e-beam evaporation machine (i). The wafer will subsequently be lifted off in Acetone for several minutes to remove redundant metal. Finally, the electrodes will be annealed at $460\text{ }^{\circ}\text{C}$ for 20s with a nitrogen flow rate at $20\text{cm}^3\text{s}^{-1}$, in order to obtain a good Ohmic contacts. After wire – bonding, the whole QDIP chip fabrication is finished. All kinds of characteristics of QDIP chips can be tested in the CEMOS lab.

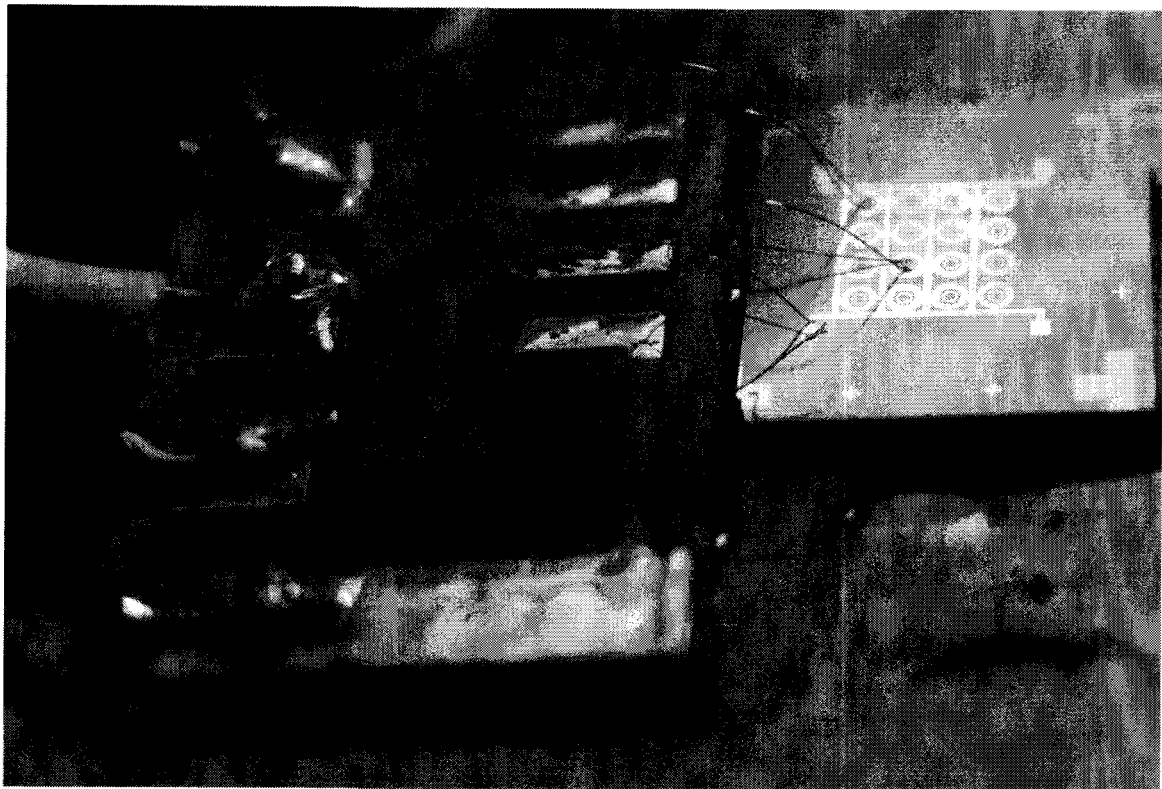


Figure 11 QDIP devices with wire bondings

III. Device Characterization

3.1 Fourier Transform Infrared (FTIR) test

3.1.1 FTIR test set up

FTIR refers to Fourier Transform InfraRed, a common technology used to obtain the infrared spectrum. In FTIR spectroscopy, some of the IR radiations transmit the sample, and others are absorbed by the wafer. Since the absorption signals convey the vibration frequencies between the atom bonds of the material, and no two materials have the same atom composite, the resulting infrared spectrum is always unique. With advanced software algorithms, FTIR spectroscopy is a very useful instrument for quantitative analysis of different materials.

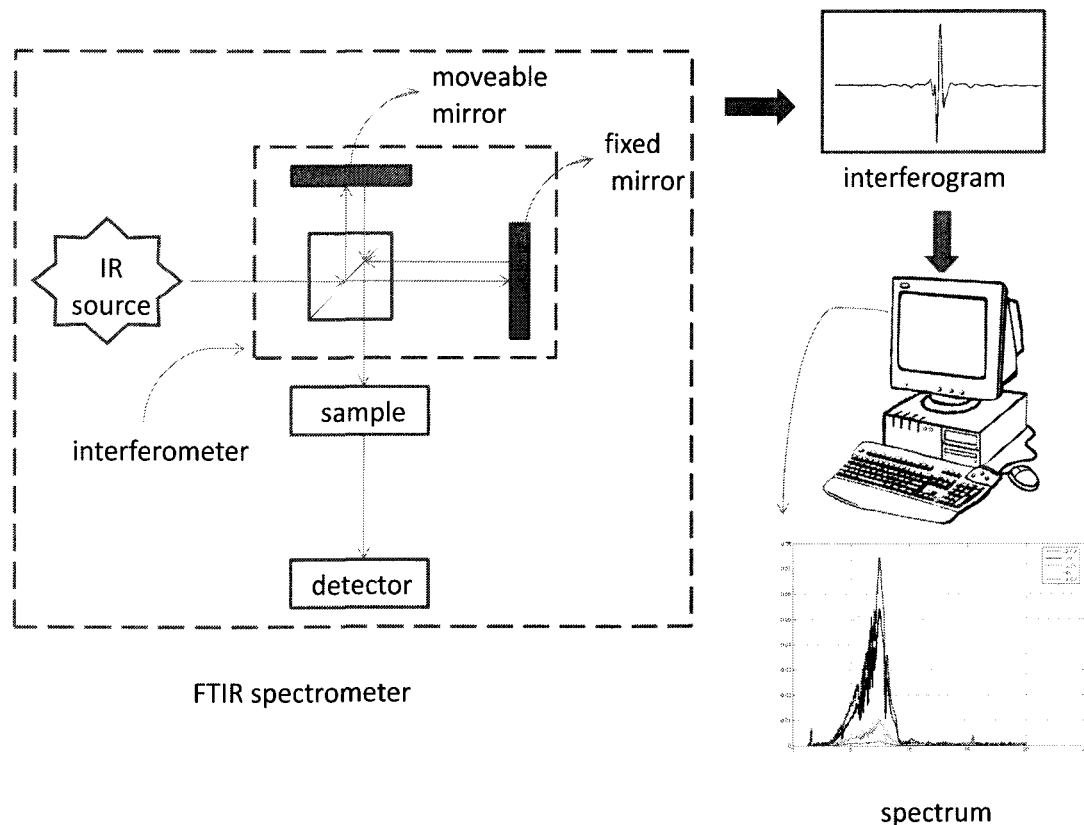


Figure 12 Schematic Illustration of FTIR System

The standard steps for FTIR test is as follows: passing through a beamsplitter, an incident IR beam is divided into two beams. One beam reflects from a fixed mirror, and the other reflects from a moveable mirror. The two reflection beams are recombined again in the beamsplitter. Since the two beams have traveled a different distance, they begin to interfere each other, and resulting an interferogram, which contains infrared frequency information. Then the interferogram signal will propagate and meet the sample surface. During the process of transmission or reflection, energy with specific frequencies will be absorbed due to the excited vibration of function groups in molecules. After interaction with the sample, the beam will be received by the detector. The detected interferogram has to be processed by computer first. According to the well-known mathematical technique – Fourier transformation, we can get infrared spectrums concerning information about absorbance (or transmittance) versus wave number.

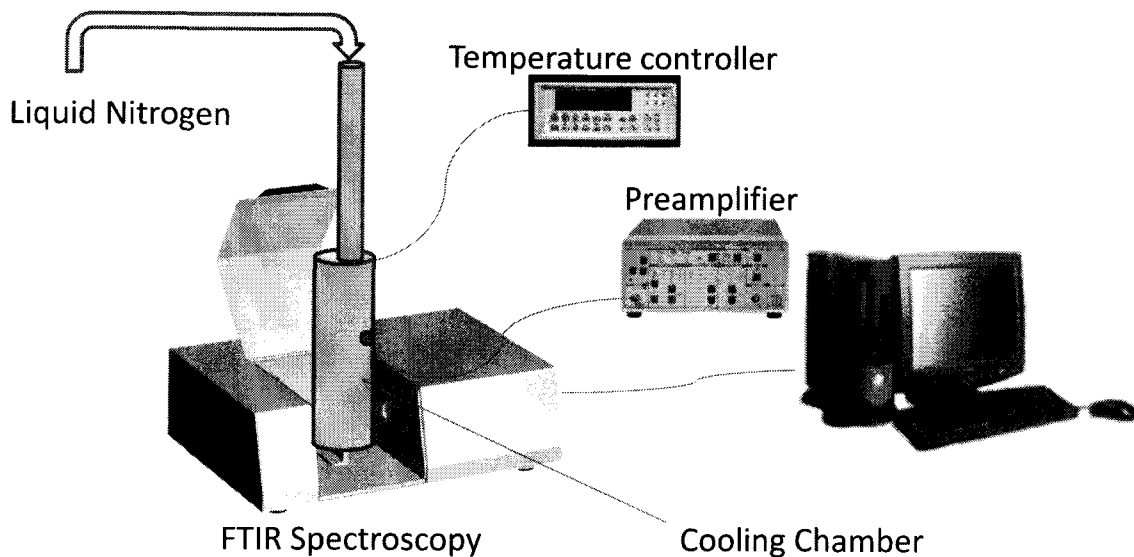


Figure 13 FTIR test set up in CEMOS lab

The set up of FTIR test is illustrated in the figure 13. The QDIP sample is fixed inside a cooling chamber (Janis, model No: ST - 100), which is embedded in the FTIR body, so that the IR beam can propagate to the QDIP sample through ZnSe windows. The temperature within the chamber is manipulated by a temperature controller (Lakeshore, 331 Temperature Controller) with the nitrogen gas supply system. During the test, bias voltage is applied on the sample by preamplifier(Stanford research systems, model SR570).

3.1.2 FTIR test result

The FTIR performance for sample #2797 is shown below:

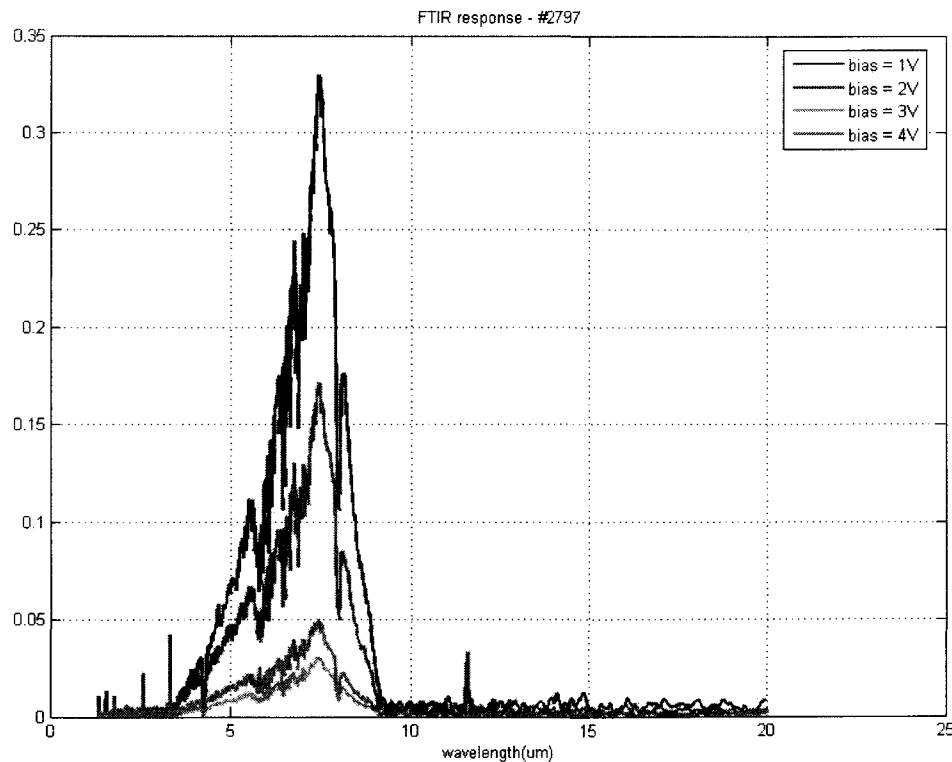


Figure 14 FTIR response for sample #2797 under 78K – positive bias

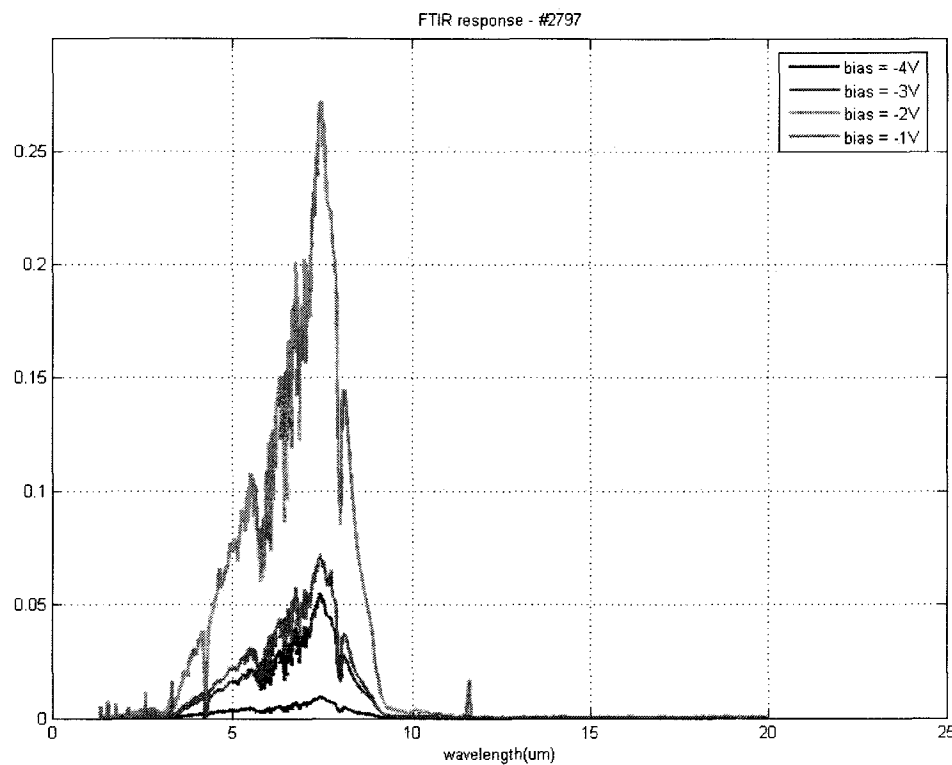


Figure 15 FTIR response for sample #2797 under 78K – negative bias

According to the FTIR performance, the absorption signal mainly falls on the wavelength range (half bandwidth) between 6.8 um and 8 um, which substantiate the PL measurement result in Chapter 2.2.

3.2 Dark Current test

3.2.1 Dark Current test set up

Dark current refers to the small electric flow in the QDIP device while no light source is introduced. Physically, with applied bias voltage, the electron and hole pairs inside the material will randomly generate and form a small electric current. The dark current generates from the following aspects: 1. thermionic emission; 2. low bias sequential resonant tunneling; 3. phonon assisted tunneling(15).

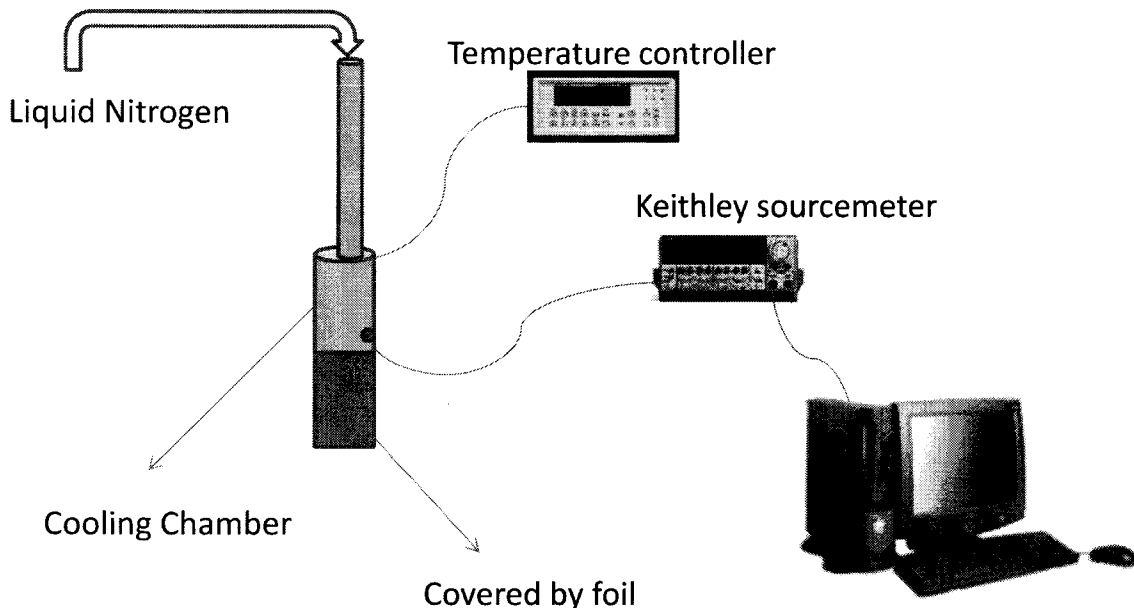


Figure 16 Dark current test set up in CEMOS lab

Figure 16 presents the set up of dark current test in CEMOS lab. The QDIP device is still placed inside a cooling chamber (Janis, model No: ST 100), while the window area is covered with foil to prevent the contact between the QDIP device and outside light

source. The temperature inside the chamber is maintained at 78K by the temperature controller (Lakeshore, 331 Temperature Controller) with the nitrogen gas supply system. The dark current is measured by the Keithley 2602 system sourcemeter. By applying the bias voltage (from -5 V to 5 V with the step of every 0.01 V) on the QDIP device, and collecting the corresponded current, the I-V characteristics can be obtained at last. The whole test is processed in a dark room in order to increase accuracy.

3.2.2 Dark current test result

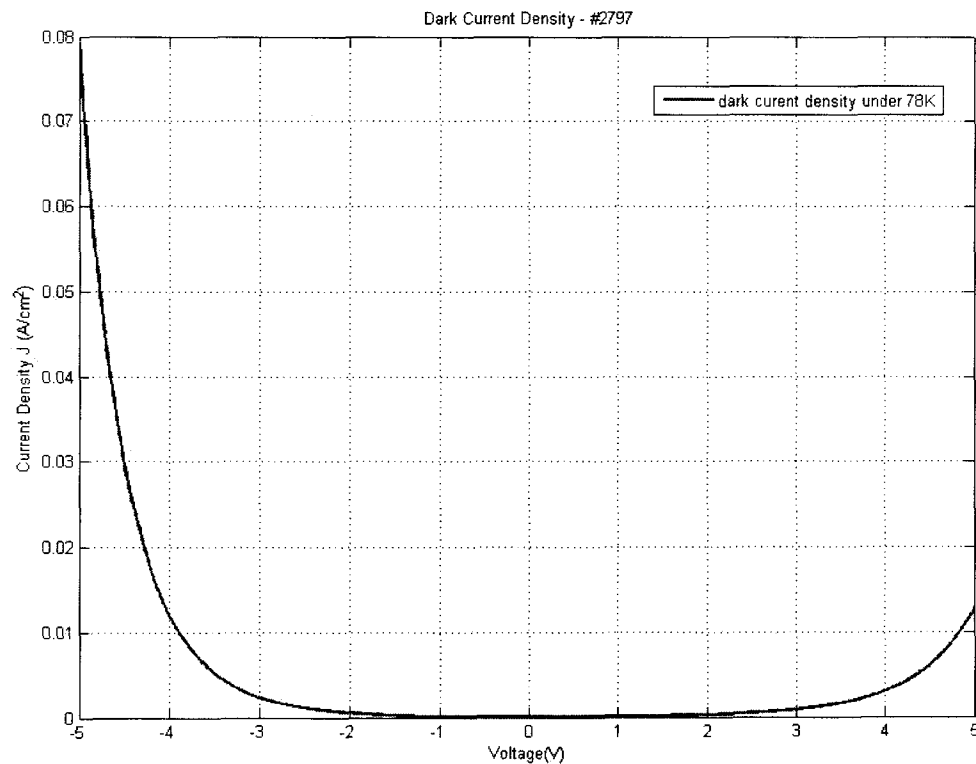


Figure 17 Dark Current Density for #2797 – linear scale

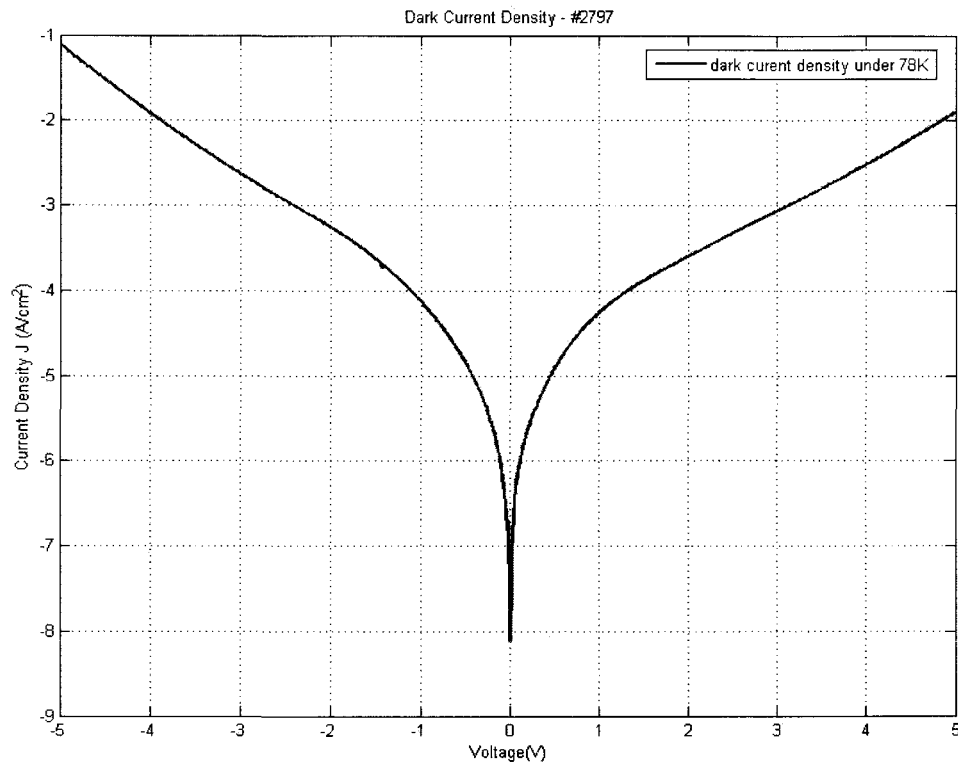


Figure 18 Dark Current Density for #2797 – log scale

The dark current density can be calculated using the equation $J = I_{\text{dark}} / A$, where A is the opening area of the device. In sample #2797, the dimension of the circular mesa is 250 μm in diameter.

As what is shown in figure 17 and figure 18, the dark current rise up rapidly with the increasing bias. The reason is as follows: at the beginning, more electrons will occupy the quantum dots with increasing bias, causing an increase in the average sheet electron density; when a large fraction of QDs are occupied, further increase in the bias won't affect the sheet electron density but lower the energy barrier, causing an exponential increase in the dark current.

3.2.3 Noise current test

Noise refers to an electrical output other than the desired signal, which is a random nature of the motions of the charge carriers. In QDIPs, there are two major noise sources: Johnson noise and generation-recombination (GR) noise. Johnson noise is also known as thermal noise, which could be expressed as $i_{th}^2 = \frac{4kT}{R} \cdot \Delta f$, where k is the Boltzman constant, T is the temperature of the resistor, R is the resistance, and Δf is the noise bandwidth; GR noise comes from the random generation and recombination of the carriers, which could be expressed as $i_{GR}^2 = 4IeG \cdot \Delta f$, where I is the dark current, and G is photoconductive gain. Therefore, the total noise could be described as

$$i_N^2 = (4IeG + \frac{4kT}{R}) \cdot \Delta f$$

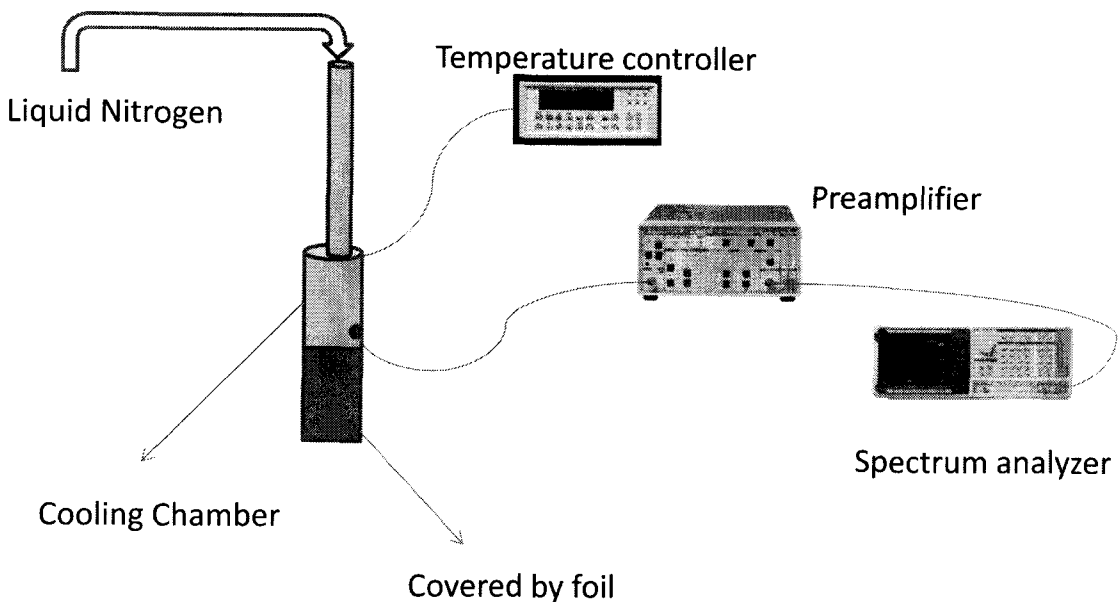


Figure 19 Noise current test set up in CEMOS lab

The noise signal is measured by a spectrum analyzer with Fast Fourier Transformation technology. In order to avoid 1/f noise, the current at the frequency of 1000 Hz will be extracted for generation-recombination (GR) noise analysis (16, 17). As shown in figure 19, the noise current test set up is similar as dark current test set up. But Keithley sourcemeter is replaced by preamplifier (Standford research system, model SR570) and spectrum analyzer (Standford research system, model SR760 FFT spectrum analyzer). During the test, preamplifier applies the bias voltage on the QDIP device, and collect the current signal. The current signal will be amplified and sent to the spectrum analyzer. By Fast Fourier Transformation, the spectrum analyzer will record noise current over a broad frequency band.

The data of dark current (absolute value) and noise current (at 1000 Hz) under different biases are recorded in the table below:

Bias(V)	-4.8	-4.6	-4.4	-4.2	-4
Noise Current (A/VHz)	5.44E-12	4.56E-12	4.74E-12	3.60E-12	3.00E-12
Dark Current(A/cm ²)	2.58E-05	1.76E-05	1.22E-05	8.59E-06	6.01E-06
Bias(V)	-3.8	-3.6	-3.4	-3.2	-3
Noise Current (A/VHz)	2.10E-12	2.12E-12	2.18E-12	1.66E-12	1.10E-12
Dark Current(A/cm ²)	4.24E-06	3.02E-06	2.13E-06	1.60E-06	1.16E-06
Bias(V)	-2.8	-2.6	-2.4	-2.2	-2
Noise Current (A/VHz)	9.30E-13	7.00E-13	5.30E-13	7.12E-13	5.08E-13
Dark Current(A/cm ²)	8.44E-07	6.40E-07	4.74E-07	3.66E-07	2.69E-07
Bias(V)	-1.8	-1.6	-1.4	-1.2	-1
Noise Current (A/VHz)	5.12E-13	3.32E-13	3.18E-14	3.00E-14	2.40E-14
Dark Current(A/cm ²)	1.93E-07	1.39E-07	9.20E-08	5.93E-08	3.59E-08

Bias(V)	-0.8	-0.6	-0.4	-0.2	
Noise Current (A/VHz)	3.22E-14	2.00E-15	2.00E-15	2.36E-15	
Dark Current(A/cm^2)	2.00E-08	1.04E-08	4.26E-09	1.29E-09	
Bias(V)	0.2	0.4	0.6	0.8	1
Noise Current (A/VHz)	2.27E-15	2.31E-15	2.91E-15	2.53E-14	2.60E-14
Dark Current(A/cm^2)	1.20E-09	4.00E-09	9.11E-09	1.71E-08	2.77E-08
Bias(V)	1.2	1.4	1.6	1.8	2
Noise Current (A/VHz)	3.72E-14	3.45E-14	3.98E-14	3.62E-14	3.12E-13
Dark Current(A/cm^2)	4.05E-08	5.59E-08	7.43E-08	9.69E-08	1.25E-07
Bias(V)	2.2	2.4	2.6	2.8	3
Noise Current (A/VHz)	3.34E-13	4.76E-13	4.59E-13	6.19E-13	6.89E-13
Dark Current(A/cm^2)	1.61E-07	2.06E-07	2.63E-07	3.36E-07	4.28E-07
Bias(V)	3.2	3.4	3.6	3.8	4
Noise Current (A/VHz)	1.06E-12	8.97E-13	1.16E-12	1.27E-12	3.03E-12
Dark Current(A/cm^2)	5.47E-07	6.99E-07	8.97E-07	1.16E-06	1.51E-06
Bias(V)	4.2	4.4	4.6	4.8	
Noise Current (A/VHz)	3.49E-12	3.93E-12	4.94E-12	7.33E-12	
Dark Current(A/cm^2)	1.95E-06	2.62E-06	3.45E-06	4.61E-06	

Table 2 test data for #2797 under 78 K

3.3 Photocurrent test

3.3.1. Photocurrent test set up

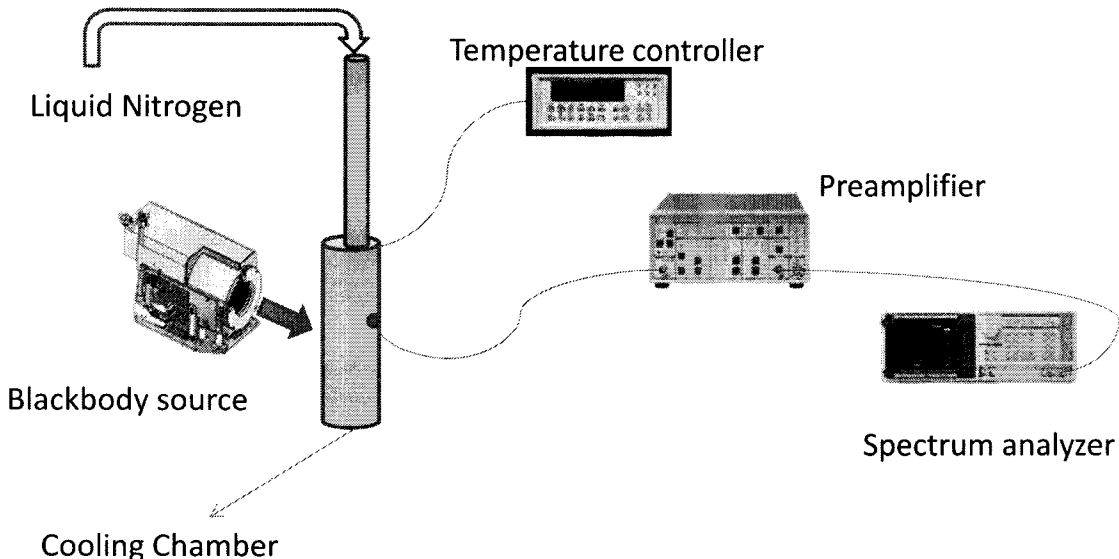


Figure 20 Photocurrent test set up in CEMOS lab

As what is displayed in figure 20, the set up of photocurrent test is similar as that of noise current test, but the foil is removed, and a blackbody source (SBIR, Santa Barbara Infrared INC.) is introduced in the system. An internal chopper is set inside the blackbody source which shuffles at a frequency of 1000 Hz. The modulated light will first pass through an optical in order to filter the spectrum into a perfect infrared, then reach the QDIP device through a ZnSe window. The infrared radiation will cause photoexcitation of the electrons inside the QDIP device, and generate photocurrent signal, which will be amplified by the preamplifier and then sent to the spectrum analyzer. The reason to select 1000 Hz modulation is to reduce 1/f noise, same as what we did in the noise current test.

3.3.2. Photocurrent test results:

The photocurrent data for #2797 under 78K is shown below. The temperature of the black body source is set at 1000 °C, the aperture is set at 78 mm² and the distance between the blackbody and the QDIP device is about 8 inches.

Bias(V)	-4.8	-4.6	-4.4	-4.2	-4
Photocurrent(A)	4.50E-08	4.02E-08	3.56E-08	3.19E-08	2.89E-08
Bias(V)	-3.8	-3.6	-3.4	-3.2	-3
Photocurrent(A)	2.61E-08	2.36E-08	2.14E-08	1.93E-08	1.75E-08
Bias(V)	-2.8	-2.6	-2.4	-2.2	-2
Photocurrent(A)	1.58E-08	1.04E-08	9.28E-09	8.1E-09	6.8E-09
Bias(V)	-1.80	-1.60	-1.40	-1.20	-1.00
Photocurrent(A)	5.52E-09	4.31E-09	3.22E-09	2.34E-09	2.42E-10
Bias(V)	-0.8	-0.6	-0.4	-0.2	
Photocurrent(A)	1.69E-10	1.12E-10	6.44E-11	1.52E-12	
Bias(V)	0.2	0.4	0.6	0.8	1
Photocurrent(A)	1.08E-12	4.81E-11	8.37E-11	1.27E-10	1.75E-10
Bias(V)	1.2	1.4	1.6	1.8	2
Photocurrent(A)	2.24E-10	1.88E-09	2.25E-09	2.63E-09	3.06E-09
Bias(V)	2.2	2.4	2.6	2.8	3
Photocurrent(A)	3.52E-09	3.97E-09	4.49E-09	5.03E-09	5.64E-09
Bias(V)	3.20E+00	3.40E+00	3.60E+00	3.80E+00	4.00E+00
Photocurrent(A)	6.38E-09	7.17E-09	1.12E-08	1.25E-08	1.39E-08
Bias(V)	4.2	4.4	4.6	4.8	
Photocurrent(A)	1.54E-08	1.69E-08	1.85E-08	2.04E-08	

Table 3 test data for #2797 under 78K

3.4 Photoconductive Gain

In QDIP device, an electron-hole pair will be generated by photoexcitation. Since electron moves faster than hole, the power source will supply another electron into the circuit. The supplement won't be stopped until the electron is captured by the hole.

Generally speaking, the photoconductive gain is equal to the number of electrons collected between the generation and recombination period of an electron-hole pair.

Detailed explanations are expressed in the following pictures.

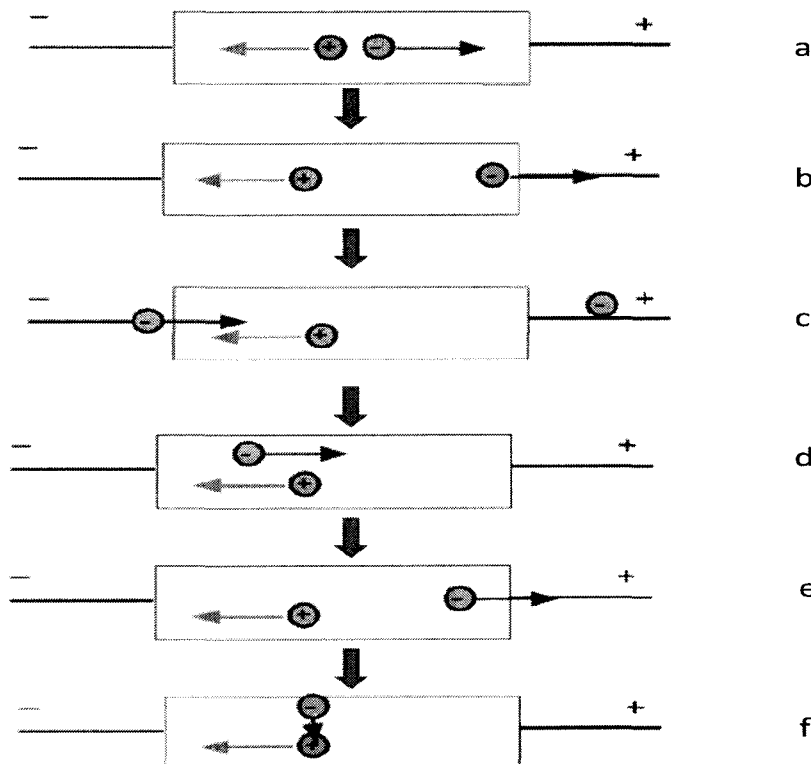


Figure 21 Explanation for Photoconductive Gain

In a conventional photoconductor, the photoconductive gain and the noise gain are equal, so that it can be calculated by the equation below:

$$G_n = \frac{i_{noise}^2 - 4kT/R}{4eI_{dark}} \quad (3.1)$$

Where i_{noise} is the noise current

i_{dark} is the dark current

e is the electron charge

k is Boltzmann's constant

T is temperature (in Kelvin)

R is the differential resistance of the photodetector

The gain for #2797 can be calculated by equation 3.1, basing on the data in table 3.1, assuming G – R noise dominates (18). The result is attached below:

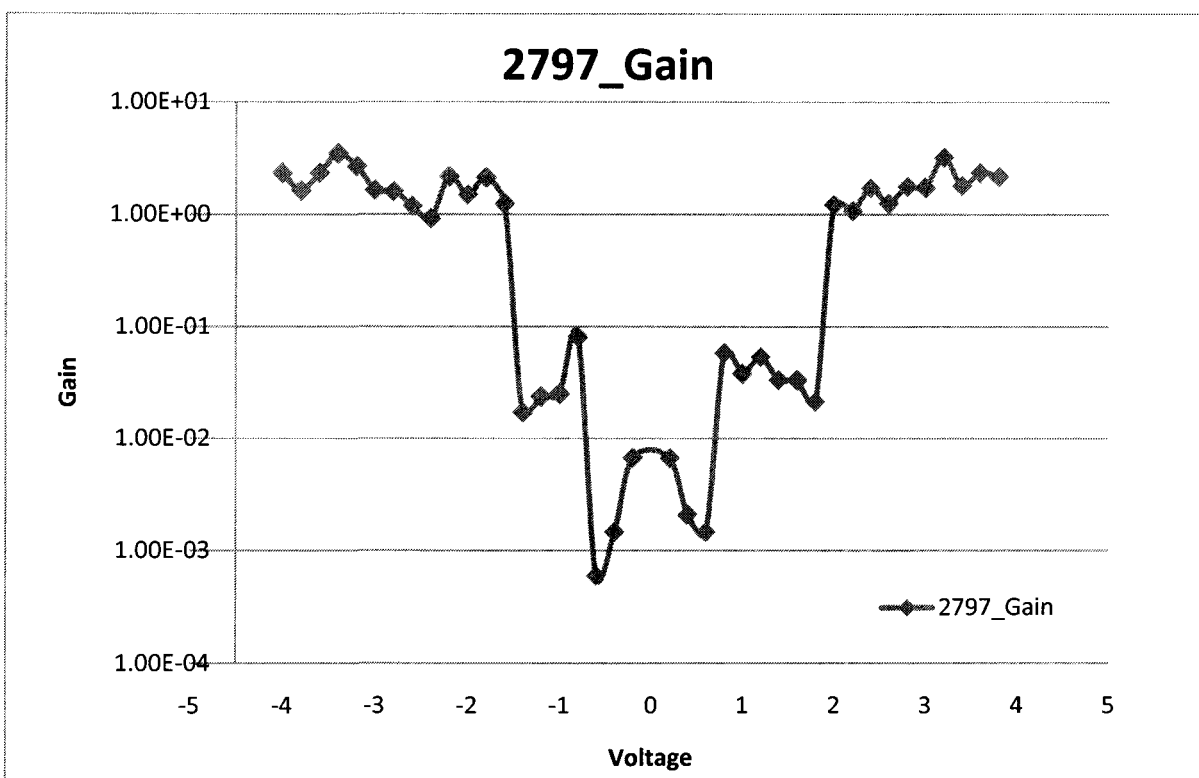


Figure 22 Conductive gain for #2797 under 78K`

3.5 Photoresponsivity

Responsivity characterizes the input – output gain of a detector system. In the specific case of photodetector, responsivity is defined as photocurrent per unit watt of incident light at a specific wavelength range. It can be described by:

$$R = \frac{\text{Photocurrent (A)}}{\text{Incident Optical Power (W)}} = \frac{I_{ph}}{P_0} \quad (3.2)$$

I_{ph} is the photocurrent we obtained in table 3.2, while P_0 is the incident optical power emitted from the black body source. P_0 can be calculated by using Black body radiation calculator if some related factors are given, including the opening area of the blackbody source, solid angle in the test set up, photodetector pick-up wavenumber, transmittance of optical filter and ZnSe window.

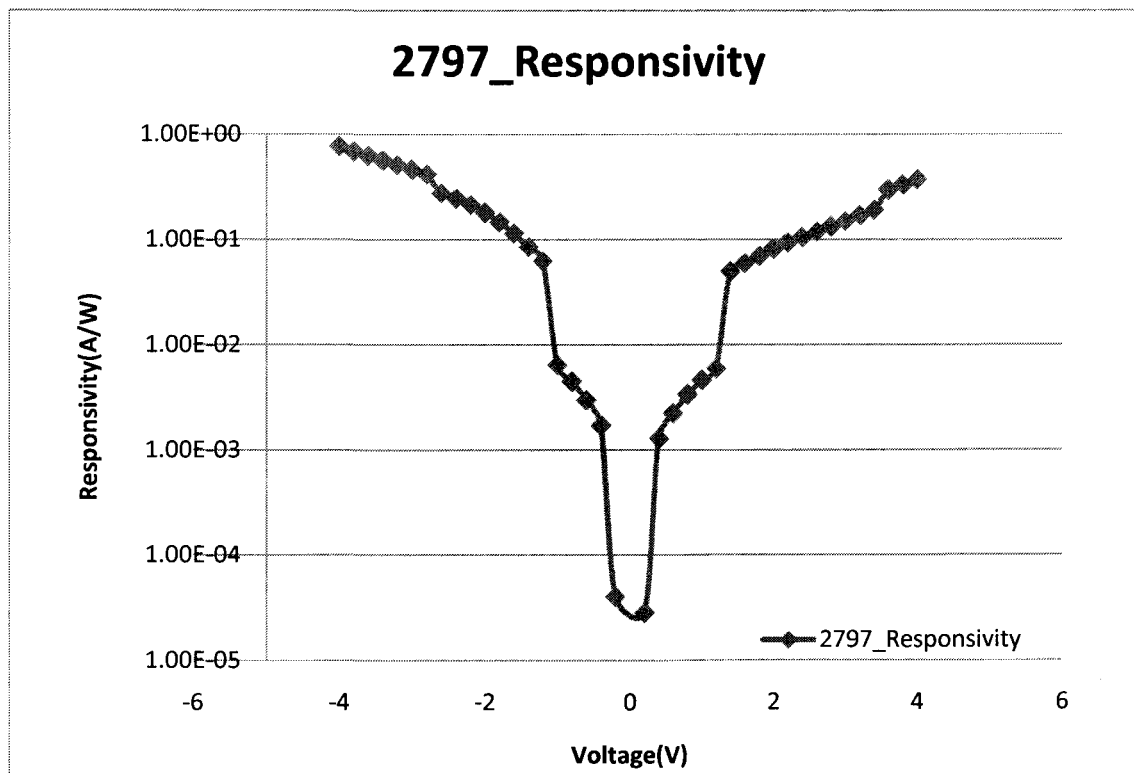


Figure 23 Photoresponsivity for #2797 under 78K

3.6 Photodetectivity

Photodetectivity is a figure of merit used to evaluate the capability of a photodetector to perceive weak signals. Therefore, a large signal always indicates a large signal to noise ratio (SNR). Photodetectivity is equal to the reciprocal of noise equivalent power (NEP). The normalized detectivity is given by:

$$D^* = \frac{\sqrt{A \cdot \Delta f}}{NEP} \quad (3.3)$$

A is the area of photosensitive region, and Δf is the effective noise bandwidth. Since NEP can be expressed as:

$$NEP = \frac{S_n \cdot \sqrt{\Delta f}}{R} \quad (3.4)$$

S_n is the noise current, and R represents for the responsivity. Substituting equation (3.4) to (3.3), a common equation for detectivity can be obtained:

$$D^* = \frac{R\sqrt{A}}{S_n} \quad (3.5)$$

The unit for detectivity is $cm \cdot Hz^{1/2}/W$.

The photodetectivity of sample 2797 is shown in figure 24. The data between -1.6V to +1.8V are eliminated, due to the limit of the measurement system. Noise current smaller than $1 \times 10^{-13} A/Hz^{1/2}$ could not be correctly measured in lower bias range(19).

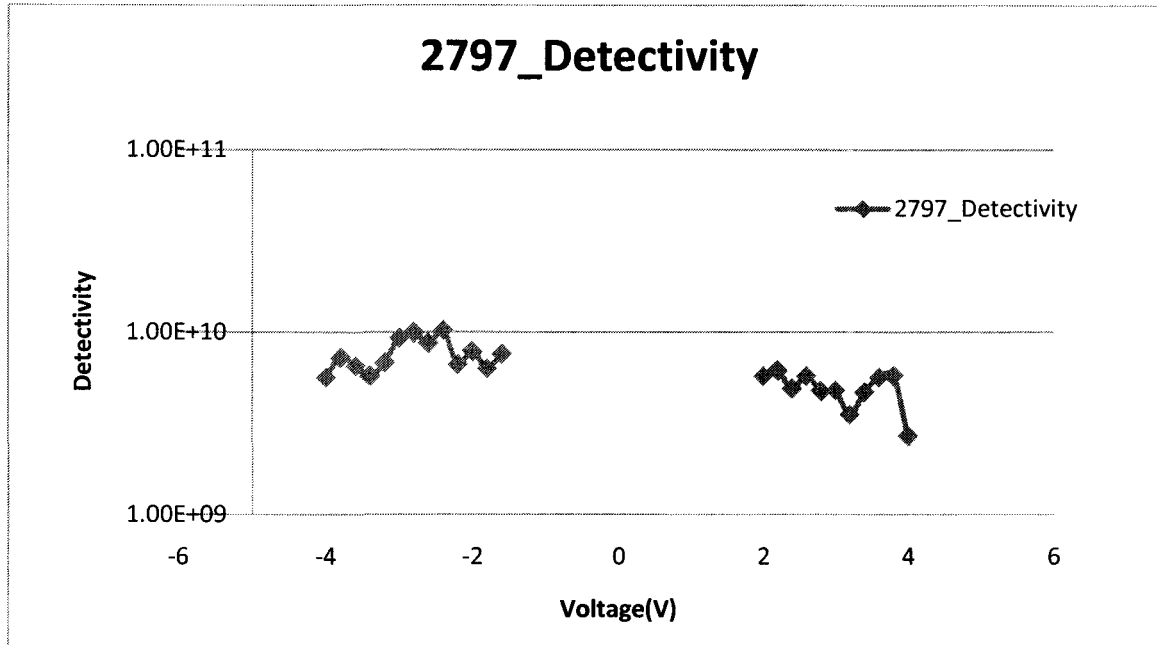


Figure 24 Detectivity for #2797 under 78K

3.7 Quantum Efficiency

Quantum Efficiency is an important attribute while measuring device's electrical sensitivity to the light. In order to improve the signal-to-noise ratio characteristic, it is essential to improve the internal quantum efficiency(20). The main mechanism for QE is to create electron-hole pairs when photons hit the photoreactive area. The quantum efficiency refers to the ratio between electron-hole pairs and incident photons, which could be obtained by the equations below:

$$\begin{aligned}
 \text{Quantum Efficiency} &= \frac{\text{output}}{\text{input}} = \frac{\text{electrons/sec}}{\text{photons/sec}} \\
 &= \frac{\text{Current} / (\text{charge of 1 electron})}{\text{total power of photons} / (\text{energy of one photon})} \\
 &= \frac{R \cdot h \cdot v}{q \cdot G} \quad (3.6)
 \end{aligned}$$

While R is the responsivity, $h\nu$ is the incident photon energy, q is the charge of the electrons and G is the photoconductive gain. As a good approximation, the noise gain can be used instead of the photoconductive gain (Equation 3.1). Based on all the data we got before, the quantum efficiency could be determined finally. The quantum efficiency of sample 2797 under different bias is presented table 3-3, and plotted in the figure 25. Due to the relatively low noise current, the data between -1.4V and 1.8V are not reliable, thus they are eliminated. The average value of other data is around 3.21%. A peak value of 11.7% was obtained at the bias of -4.8 volts under the temperature of 78K. Comparing with a common value at 1% published in the prior reports, this result is quite promising.

Bias(V)	-4.8	-4.6	-4.4	-4.2	-4
Quantum Efficiency	1.17E-01	1.02E-01	5.74E-02	6.30E-02	5.75E-02
Bias(V)	-3.8	-3.6	-3.4	-3.2	-3
Quantum Efficiency	7.47E-02	4.72E-02	2.86E-02	3.35E-02	4.98E-02
Bias(V)	-2.8	-2.6	-2.4	-2.2	-2
Quantum Efficiency	4.59E-02	4.05E-02	4.67E-02	1.74E-02	2.11E-02
Bias(V)	-1.8	-1.6	-1.4	-1.2	-1
Quantum Efficiency	1.21E-02	1.62E-02	8.73E-01	4.59E-01	4.49E-02
Bias(V)	-0.8	-0.6	-0.4	-0.2	
Quantum Efficiency	9.71E-03	8.75E-01	2.05E-01	1.05E-03	
Bias(V)	0.2	0.4	0.6	0.8	1
Quantum Efficiency	7.49E-04	1.07E-01	2.68E-01	1.01E-02	2.15E-02
Bias(V)	1.2	1.4	1.6	1.8	2
Quantum Efficiency	1.95E-02	2.63E-01	3.14E-01	5.79E-01	1.18E-02
Bias(V)	2.2	2.4	2.6	2.8	3

Quantum Efficiency	1.51E-02	1.08E-02	1.67E-02	1.31E-02	1.52E-02
Bias(V)	3.2	3.4	3.6	3.8	4
Quantum Efficiency	9.23E-03	1.86E-02	2.24E-02	2.68E-02	6.80E-03
Bias(V)	4.2	4.4			
Quantum Efficiency	7.33E-03	8.53E-03			

Table 3-3 quantum efficiency for #2797 under 78K

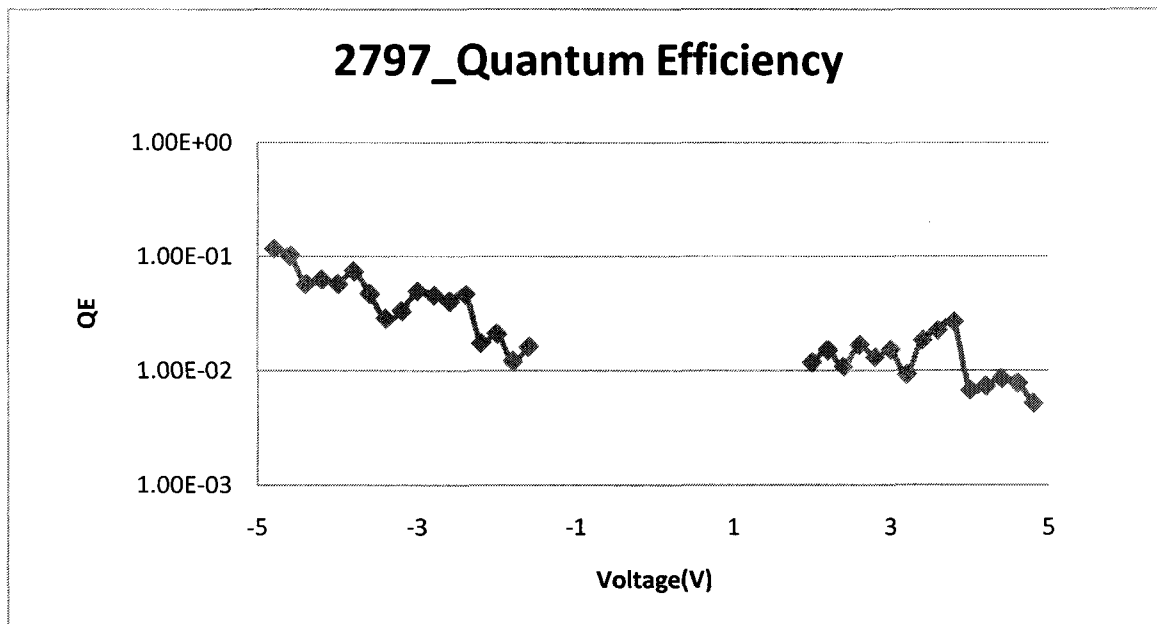


Figure 25 Quantum Efficiency for #2797 under 78K

A more direct way to explain quantum efficiency is Beer – Lambert's Law(21).

The beer's law states that there is a logarithmic relationship between the transmission T

of light travelling through an object and the product of absorption coefficient α and the distance the light travels through this object. This relation could be expressed as:

$$I_1 = I_0 \cdot e^{-\alpha L} \quad (4.3)$$

Where I_0 and I_1 are the intensity of the incident light and the transmitted light, respectively, α is the absorption coefficient of the material, and L is the path length of the object. The diagram of Beer's law is illustrated in Figure 26.

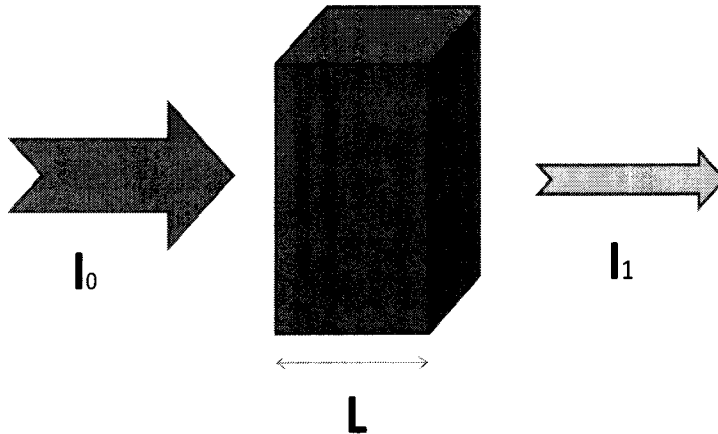


Figure 26 Diagram of Beer-Lambert absorption
(A beam of light travelling through an object with a width of L)

The relationship between I_0 and I_1 could also be written as equation 4.4, the transmitted light equals to the incident light get rid of the absorbed light.

$$I_1 = I_0(1 - QE) \quad (4.4)$$

By substituting equation 4.4 into equation 4.3, the relationship between $\ln(1-QE)$ and the bias voltage would be obtained.

$$\ln(1-QE) = -\alpha L \quad (4.5)$$

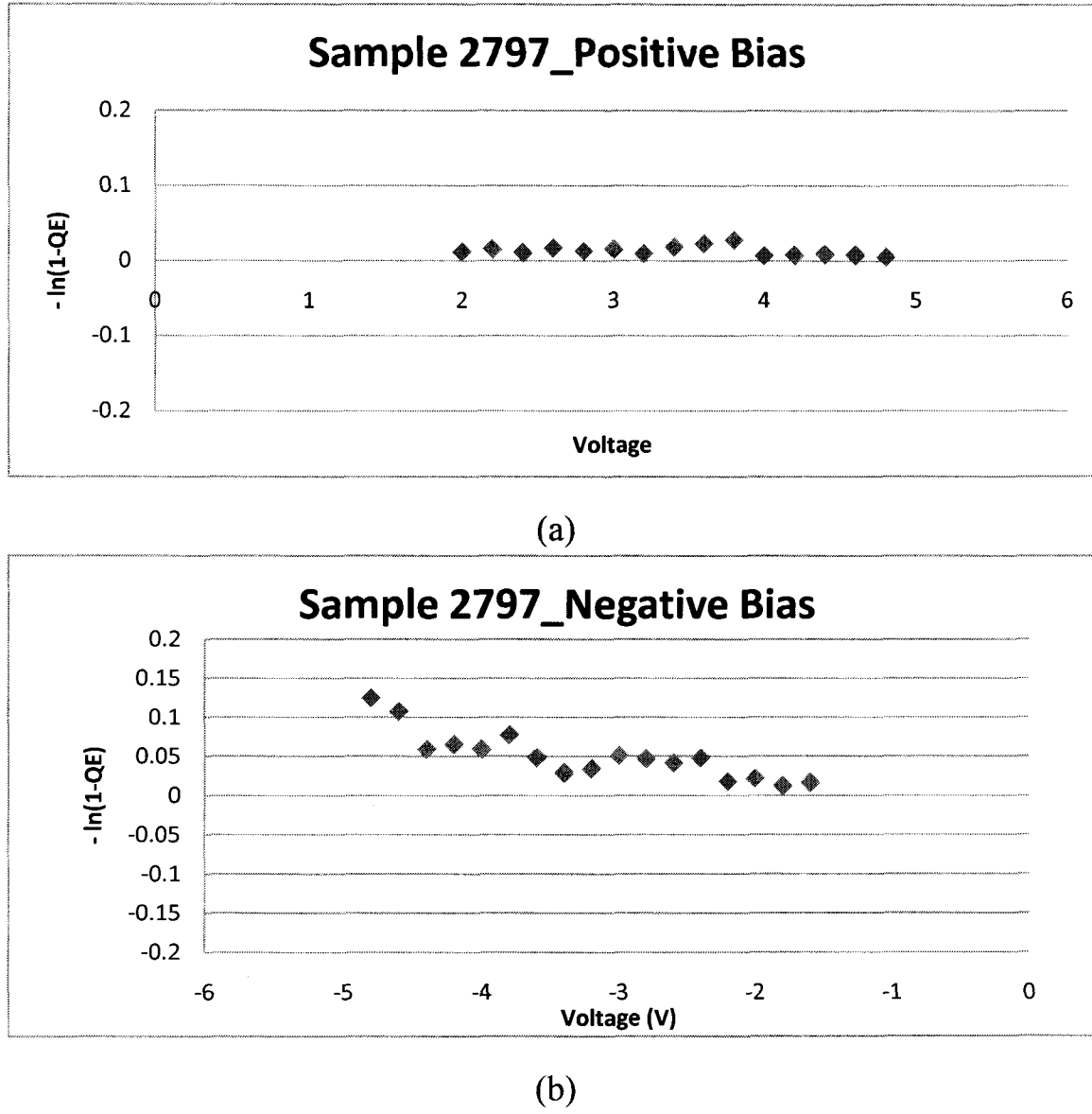


Figure 27 $\ln(1-QE)$ Vs Voltage

Based on the test data in table 3-3, the relationship between $-\ln(1-QE)$ and bias voltage was plotted in figure 27, which also indicates that although the quantum efficiency varies much with different bias voltage, the absorption coefficient can be roughly considered as the same, especially in the positive bias part and lower negative bias part.

The reason that the absorption rate appears slightly increased in the large negative bias is because the increase of the escape probability. According to B.F Levine's conclusion(10), the total net quantum efficiency could be expressed as

$$QE = \eta_a \cdot P_e \quad (4.6)$$

Where η_a is the optical-absorption quantum efficiency and P_e is the probability that a photoexcited electron will escape from the quantum well and contribute to the photocurrent, rather than being recaptured by the originating well.

B.F Levine's paper also indicates that the escape probability $P_e = (1 + \frac{\tau_e}{\tau_r})^{-1}$, while the escape time ration $\frac{\tau_e}{\tau_r} = (\frac{\tau_e}{\tau_r})_0 e^{-V/V_p}$, therefore, the escape probability and the bias voltage V now could be written as:

$$(\frac{\tau_e}{\tau_r})_0 e^{-\frac{V}{V_p}} = (P_e^{-1} - 1) \quad (4.7)$$

Where τ_e is the escape time, τ_r is the relaxation time back into the originating well, $(\tau_e/\tau_r)_0$ is the zero bias escape time ratio, and V_p is the effective barrier lowering potential per period.

By taking the ln of both sides, equation 4.7 could also be written as

$$\ln(P_e^{-1} - 1) = -\frac{V}{V_p} + \ln(\frac{\tau_e}{\tau_r})_0 \quad (4.8)$$

From equation 4.8, it is clear that $\ln(P_e^{-1} - 1)$ and the bias voltage V should have some linear relationship. Assuming the absorption coefficient does not change with the bias, quantum efficiency could be used to take the place of the escape probability to verify this relationship. This linear result could be seen in figure 28, as expected, to be in good agreement with the values obtained directly from the test data in table 3-3.

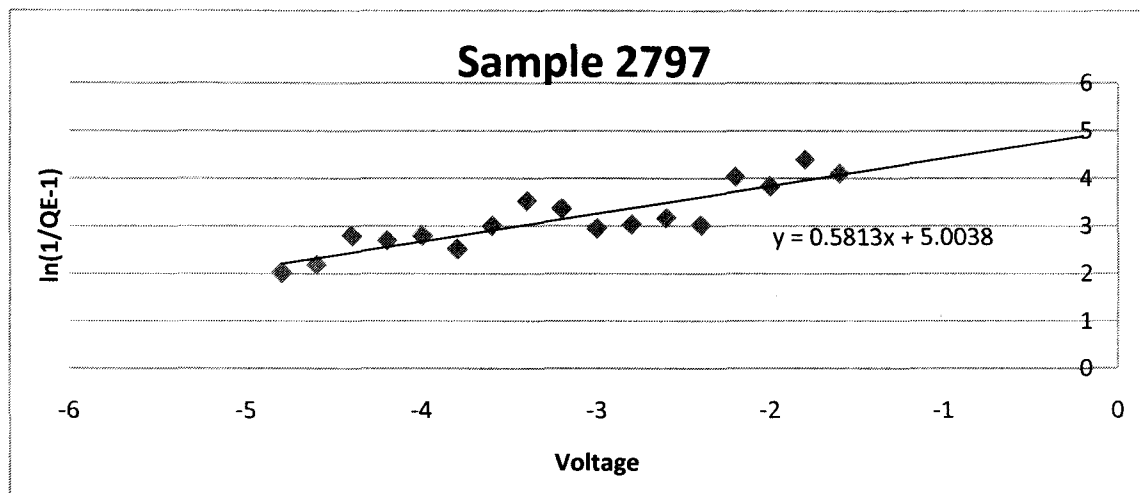


Figure 28 $\ln(1/QE-1)$ Vs Voltage

According to Equation 4.8 and Figure 28, the conclusion could be drawn. The quantum efficiency is related with optical absorption coefficient and the escape probability. The formal could be considered as constant, while the latter will become larger with a higher bias voltage.

This conclusion is consistent with what is shown in figure 27 (b). While the bias voltage is small, the effect of escape probability could be neglected, so that the net quantum efficiency is almost a constant. However, when the bias voltage increases to a certain value where the escape probability takes a great influence, the total net quantum

efficiency will rise with the bias voltage. The reason that the quantum efficiency under the positive bias (in figure 27 (b)) seems to be independent with the voltage is because the existence of a barrier layer, which could help to eliminate the influence of the escape probability. This could be illustrated in the figure 29.

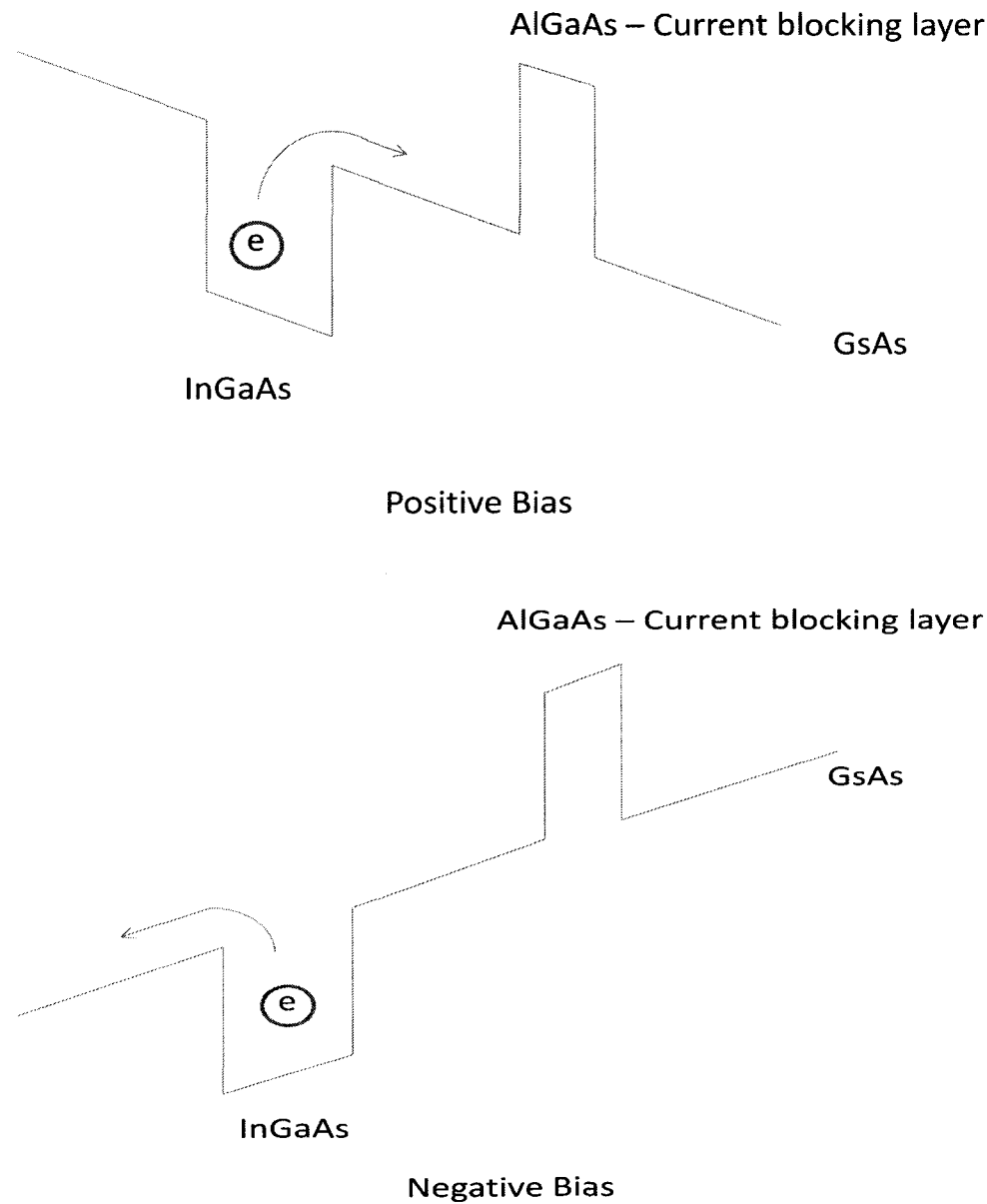


Figure 29 Diagram of the QDIP with bias voltage

The results shown in figure 27 and figure 28 substantiate the initial assumption, which also indicates that the quantum efficiency obtained in this thesis is reliable and reasonable.

IV. Comparison and Discussion

4.1 10-period sample #2783

In order to better evaluate all the characteristics for 20-period sample #2797, a 10-period sample #2783 is introduced here to make a comparison. All the growth, fabrication and test conditions are the same between those two samples. The only difference is the growth structure, which is displayed below:

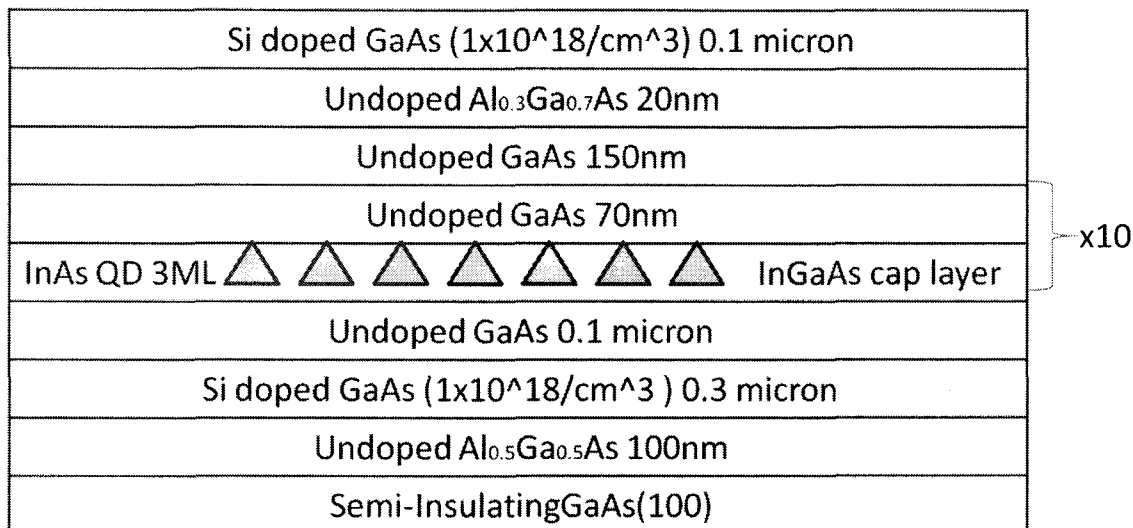


Figure 30 the schematic structure for 10-layer sample #2783

The 0.1 micron Si doped GaAs is the top contact layer while 0.3 micron Si doped GaAs is the bottom contact layer; the 20nm undoped Al_{0.3}Ga_{0.7}As is a barrier layer in order to block the dark current flow; the 0.15 micron undoped GaAs layer and 0.1 micron undoped GaAs are diffusion layers, used to prevent the silicon dopants diffuse to the 10 period InAs quantum dots layer between them; the 100 nm undoped Al_{0.5}Ga_{0.5}As is a selective etching layer which could be used in the fabrication of focal plane array; the semi-insulating GaAs layer is the substrate.

Compared with Figure 7, it is easy to sum up the thickness of each sample (from top contact layer to bottom contact layer), which are 2370.1nm and 1378.55nm separately, assuming 1 ML InAs quantum dots is equal to 0.285nm. Since the bias voltage is applied between these two contact layers, the electric field of #2783 is approximately twice as the electric field of #2797 under the same bias voltage.

4.2 FTIR Performance:

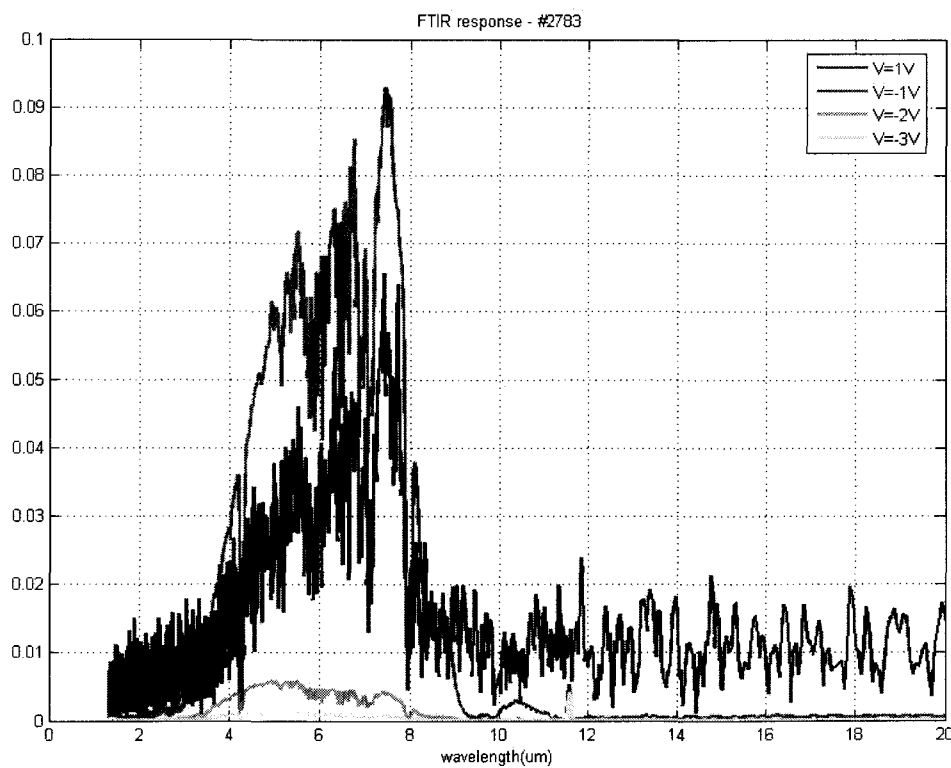


Figure 31 FTIR response for sample #2783 under 78K

According to the picture above, it is clear that the peak wavelength range for #2783 is about 6-8 um, which is similar with #2797, as shown in Fig3.3 and Fig 3.4. Under the same testing environment, the blackbody radiation power can be considered as the same.

The major difference between these two samples is the repeating times of the quantum dots layers. By comparing each characteristics separately, the effect of more quantum dots layers could be well determined.

4.3 Dark Current Comparison

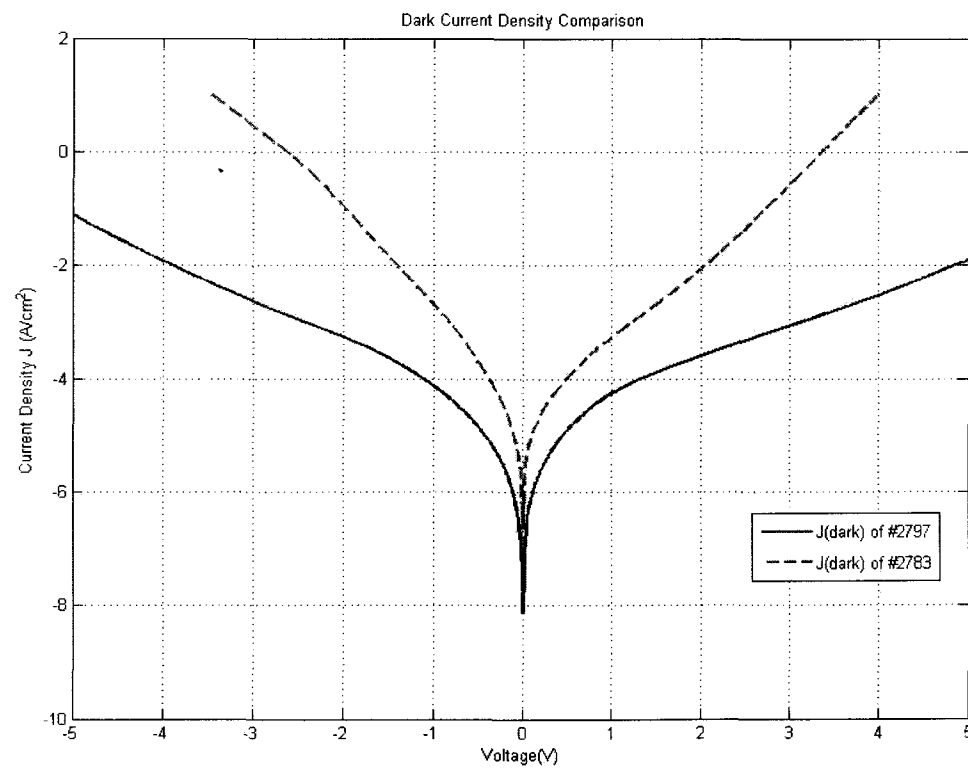


Figure 32 Dark current comparison

From the figure shown above, it is obvious that the dark current density of #2797 is lower than that of #2783. This result is as expected and can be explained from the equations below:

$$J = n \cdot v \cdot q \quad (4.1)$$

where J is the dark current density, n is charge carrier density, v is the drift velocity and q is the charge on each particle. The average drift velocity can be expressed as

$$v = \mu \cdot E = \mu \cdot V / L \quad (4.2)$$

where μ is the electron mobility and E is the electric field. Assuming the charge carrier density and electron mobility could be considered as the same in the two devices, the only difference relies on the electric field. Since the applied voltage is the same, the longer the device is, the weaker the electric field would be, and thus the lower the dark current density would be.

Another easier explanation is: 20-period-sample can be considered as two 10-period-samples connected in series. Since the bias voltages are the same, the dark current decreases while the resistance increases.

4.4 Photoconductive gain comparison:

In order to better evaluate the photoconductive gain of sample #2783 and #2797, the factor of electric field should be well considered. In this situation, electric field is introduced to take the place of the bias voltage as the x-axis, by dividing the total thickness of each QDIP, which is 2370.1nm for 20-layer QDIP and 1378.55 nm for 10-

layer QDIP specifically. From the results below, it is clearly that the gain of #2783 is higher than that of #2797, which means 10-period sample has a lower electron capture probability. This is easy to imagine since 20-period sample has more quantum dots, hence the probability to capture an electron is larger than 10-period sample.

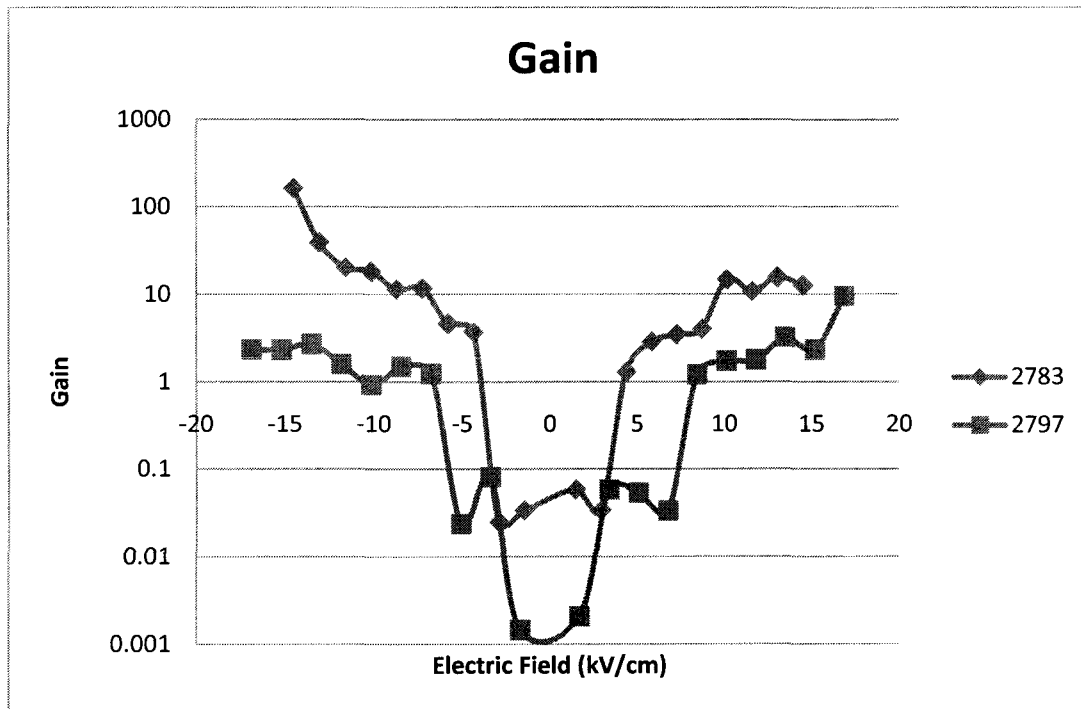


Figure 33 Photoconductive Gain Comparison

4.5 Photoresponsivity Comparison

After normalizing the electric field for #2797 and #2783, it is interesting to find that the photoresponsivities of these two samples are well overlapped. This is easy to explain. From Chapter 4.1, it is clear that these two samples have almost the same peak half bandwidth wavelength, and the same testing environment, so that the BBR powers for the two samples are the same. Meanwhile, based on Equation 4.1 and 4.2 the photocurrent is also equivalent due to the same charge carrier density, electron mobility

and normalized electric field. This well overlapped figure also indicates that the data is accurate and reliable.

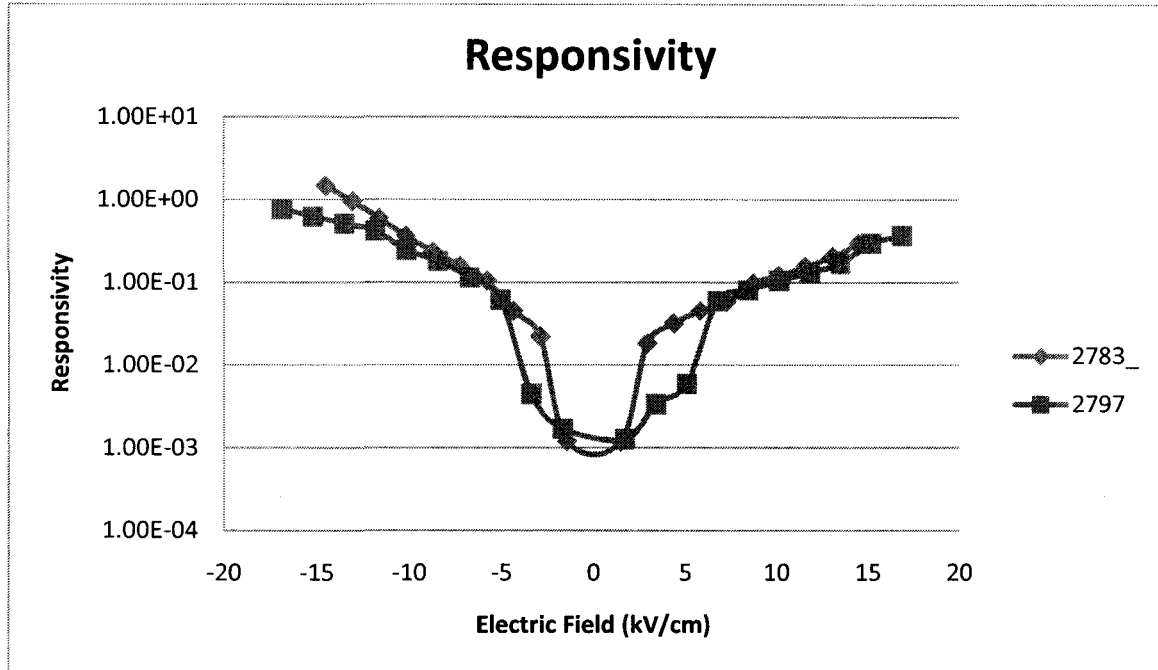


Figure 34 Responsivity Comparison

4.6 Photodetectivity Comparison

In Figure 35, the detectivity of sample 2783 and 2797 are also placed together based on the electric field. It is obvious that the detectivity of 20 layers is larger than that of 10 layers sample. According to the equation 3.5, the detectivity is related with the responsivity, photosensitive area and noise current. Since these two samples are fabricated with the same photolithography mask, the photosensitive area should be identical; meanwhile, the responsivity could also be considered as the same according to

Figure 34, so the difference is decided by the noise current. Based on the explanation in Chapter 3.2.2, the noise current for sample #2797 is much lower than that of #2783. Therefore, the photodetectivity of sample #2797 is much higher.

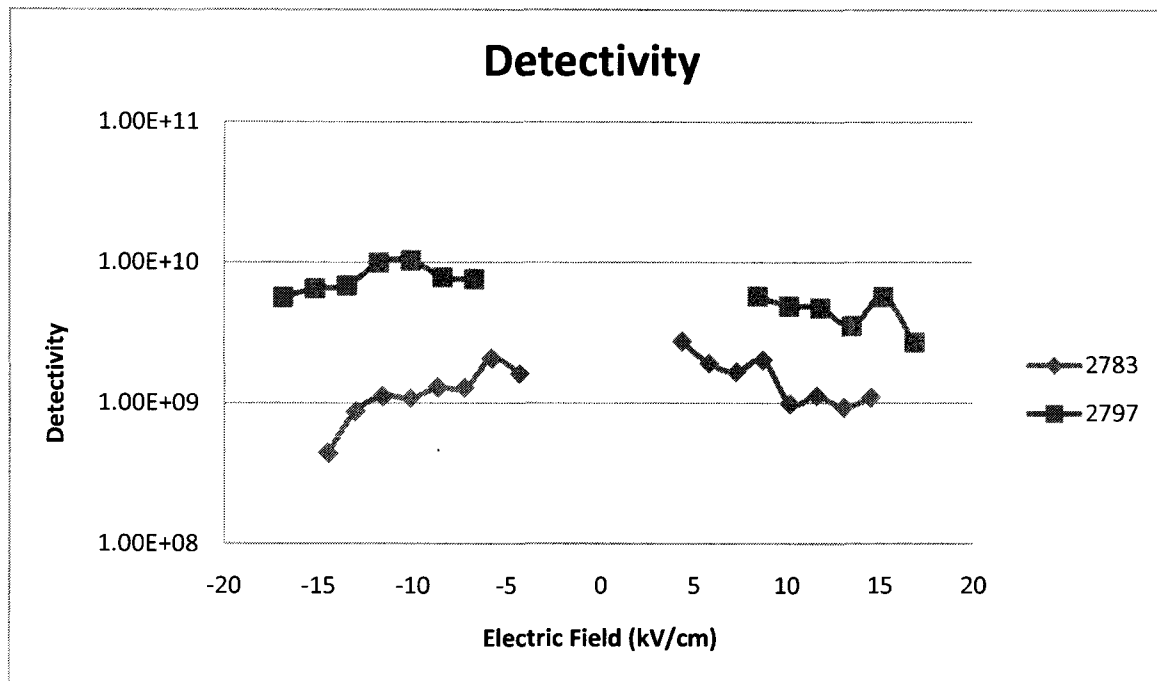


Figure 35 Photodetectivity Comparison

4.7 Quantum Efficiency Comparison

The quantum efficiency is also compared under the same electric field in Figure 36. A much higher quantum efficiency was obtained in the twenty period sample. The average quantum efficiency is around 1.039% for #2783 while it is around 3.21% for #2797. This is a good results comparing with a common value at 1% published in the prior reports(11). The reason for the difference between these two samples can be well explained by the Beer's Law (Equation 4.3).

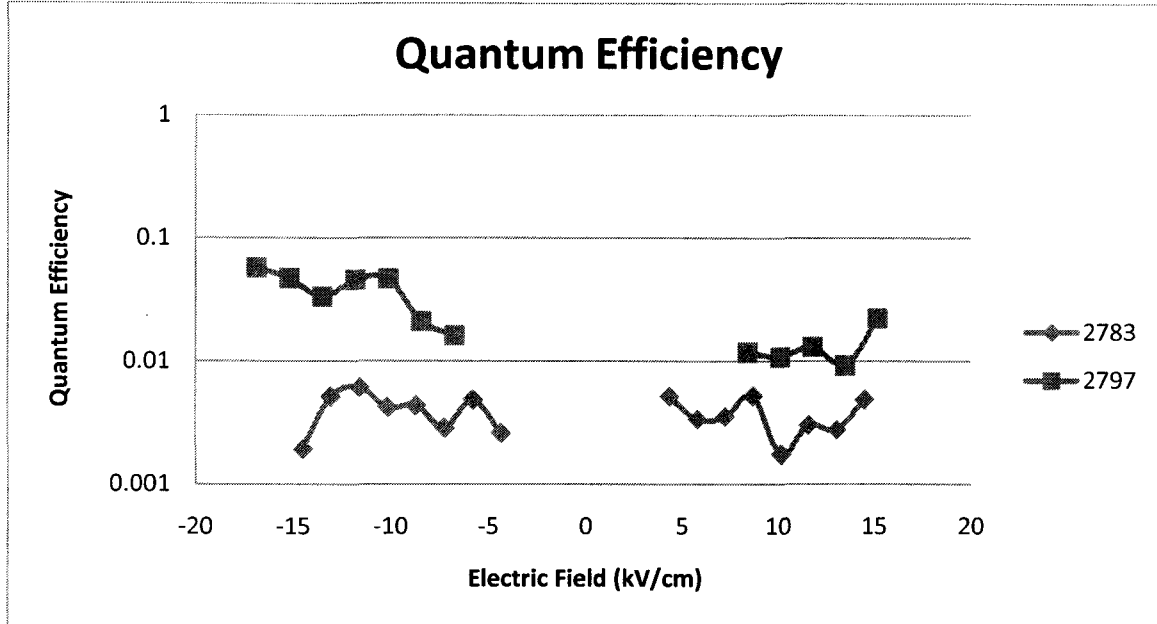


Figure 36 Quantum Efficiency Comparison

Comparing with #2783, #2797 has more quantum dots layers, which leads to a larger distance L. Therefore, with the same intensity of incident light, more photons are absorbed, more electron-hole pairs are generated, and more electrons are collected as photocurrent. As a result, a higher quantum efficiency is obtained eventually. Other elements such as the fill factor(15) may also contribute to this high quantum efficiency. The fill factor is defined as the area coverage of the QDs in a QD layer, which could be estimated from atomic force microscopy data. The fill factor varies due to the variations in the QD size and density, more data will be collected to analyze the specific relationship in the future.

V. Conclusion and Future Work

Based on the testing results and analysis mentioned above, two major conclusions were conducted in this thesis,

1. Under a twenty-QD-layer structure, a QDIP with a high quantum efficiency of 11.7% was detected, comparing with a common value of 1% published in the prior reports. Taking a ten-QD-layer structure QDIP as a reference, it is obvious that with more repeated quantum dots layers, the performance of quantum dots photodetectors are effectively enhanced.
2. The absorption coefficient could be considered the same no matter how the bias voltage changes. However, while the bias voltage increases to a certain value, the effect of the escape probability could not be neglected, so that the total net quantum efficiency appears to rise with the bias voltage. The existence of a barrier layer would help to eliminate the increase of the escape probability.

The future work of this thesis will be the optimization of the numbers of quantum dots layers. In detail, a 30 layer QDIP will be studied, and the quantitative relation between the quantum efficiency and the number of QD layers will be predicted. However, there are some potential difficulties. With more repeated quantum dots layers, the strain between crystals will increase, leading to more dislocations, and the wafer will be more fragile while cooling down. Meanwhile, the time and cost for MBE growth will also increase.

VI. Literature Cited

1. Miller and Friedman, 2004, Photonic Rules of Thumb, 9780442012106.
2. General Accounting Office (GAO) 2002 Missile Defense: Review of Results and Limitations of an Early National Missile Defense Flight Test, GAO - 02 - 124 (February).
3. Guanpala S D and Bandara S V 2000 Quantum well infrared photodetector focal plane arrays Semicond. Semimetals 62 197 - 282.
4. Mooney J M, Vickers V E, An M and Brodzik A K 1997 High-throughput hyperspectral infrared camera J. Opt. Soc. Am. A 14 2951.
5. Bryant, Lynn (2007-06-11). "How does thermal imaging work? A closer look at what is behind this remarkable technology".
6. Mahulikar, S.P., Sonawane, H.R., and Arvind Rao, G. Infrared signature studies of aerospace vehicles. Progress in Aerospace Sciences, 43(7-8): p. 218-245.
7. Characteristics and use of infrared detectors, Technical Information, SD-12, Hamamatsu Corp., Cat. No. KIRD9001E03 (2004).
8. Potter, R.F. and Eisenman, W.L., 1962. Infrared Photodetectors: A Review of Operational Detectors. Appl. Opt., 1(5): p. 567-574.
9. Barve, A.V., Lee, S.J., Noh, S.K., and Krishna, S., 2009. Review of current progress in quantum dot infrared photodetectors. Laser & Photonics Reviews, 9999(9999): p. NA.
10. Levine, B.F., 1993. Quantum-well infrared photodetectors. Journal of Applied Physics, 74(8): p. R1-R81.
11. Jamie, P., 2002. Evaluation of the fundamental properties of quantum dot infrared detectors. Journal of Applied Physics, 91(7): p. 4590-4594.
12. Lu, X., Vaillancourt, J., and Meisner, M.J., 2007. A modulation-doped longwave infrared quantum dot photodetector with high photoresponsivity. Semiconductor Science and Technology, 22: p. 993-996.
13. International Union of Pure and Applied Chemistry. "photochemistry". Compendium of Chemical Terminology Internet edition.
14. P. Vasinajindakaw, Master's Thesis, "Verification and Reduction of Dark Current On Quantum Dot Infrared Photodetector", Electrical and Computer Engineering Department, University of Massachusetts at Lowell, November 2009.

15. Zhengmao Ye, Doctor's Dissertation, "Design, Fabrication and Characterization of Quantum Dots Photodetectors", The University of Texas at Austin, December, 2003.
16. Zhengmao, Y., Campbell, J.C., Zhonghui, C., Eui-Tae, K., and Madhukar, A., 2002. Normal-incidence InAs self-assembled quantum-dot infrared photodetectors with a high detectivity. *Quantum Electronics, IEEE Journal of*, 38(9): p. 1234-1237.
17. W. A. Beck, *Appl. Phys. Lett.* 63, 3589 (1993).
18. Xuejun, L., Jarrod, V., and Mark, J.M., 2007. Temperature-dependent photoresponsivity and high-temperature (190 K) operation of a quantum dot infrared photodetector. *Applied Physics Letters*, 91(5): p. 051115.
19. Ling, H.S., Wang, S.Y., Lee, C.P., and Lo, M.C., 2008. High quantum efficiency dots-in-a-well quantum dot infrared photodetectors with AlGaAs confinement enhancing layer. *Applied Physics Letters*, 92(19): p. 193506.
20. Matsukura, Y., Uchiyama, Y., Yamashita, H., Nishino, H., and Fujii, T., 2009. Responsivity - dark current relationship of quantum dot infrared photodetectors (QDIPs). *Infrared Physics & Technology*, 52: p. 257 - 259.
21. J. D. J. Ingle and S. R. Crouch, *Spectrochemical Analysis*, Prentice Hall, New Jersey (1988).

VII. Biographical Sketch of Author

The author of this thesis was born in China and grew up in Nanjing, Jiangsu Province. She received the Bachelor of Science Degree from Southeast University, Nanjing, China, in the department of Instrument Science and Technology, at the year of 2007. She then went to the University of Massachusetts Lowell to pursue a Master of Science Degree in the department of Electrical and Computer Engineering with a specific research focus on Optics. She has obtained one publication during her master's study:

"All Ink-jet-printed Carbon Nanotube Thin-Film Transistor on a Polyimide Substrate with an Ultrahigh Operating Frequency over 5 GHz" Jarrod Vaillancourt, Haiyan Zhang, Puminun Vasinajindakaw, et. al, in Applied Physics Letters (Vol.93, Issue 24).